

# THE UNUSUALLY HIGH HALO CONCENTRATION OF THE FOSSIL GROUP NGC 6482: EVIDENCE FOR WEAK ADIABATIC CONTRACTION

DAVID A. BUOTE

Department of Physics and Astronomy, University of California at Irvine, 4129 Frederick Reines Hall, Irvine, CA 92697-4575;  
buote@uci.edu

*Accepted for Publication in The Astrophysical Journal*

## ABSTRACT

Although fossil galaxy systems are thought to be very old, and thus should possess above-average halo concentrations, typically fossils have unexceptional concentrations for their masses. We revisit the massive isolated elliptical galaxy / fossil group NGC 6482 for which previous X-ray studies of a modest *Chandra* observation obtained a very uncertain, but also possibly very high, halo concentration. We present new measurements of the hot gas surface brightness, temperature, and iron abundance using the modest *Chandra* observation and a previously unpublished *Suzaku* observation, the latter of which allows the measurements of the gas properties to be extended out to  $\sim r_{2500}$ . By constructing hydrostatic equilibrium models of the gas with separate components for the gas, BCG stellar mass, and the dark matter (DM), we measure  $c_{200} = 32.2 \pm 7.1$  and  $M_{200} = (4.5 \pm 0.6) \times 10^{12} M_{\odot}$  using an NFW DM profile. For a halo of this mass, the measured concentration  $c_{200}$  exceeds the mean value (7.1) expected for relaxed  $\Lambda$ CDM halos by  $3.5\sigma$  in terms of the observational error, and by  $6\sigma$  considering the intrinsic scatter in the  $\Lambda$ CDM  $c-M$  relation, which situates NGC 6482 as the most extreme outlier known for a fossil system. We explored several variants of adiabatic contraction (AC) models and, while the AC models provide fits of the same quality as the un-contracted models, they do have the following advantages: (1) smaller  $c_{200}$  that is less of an outlier in the  $\Lambda$ CDM  $c-M$  relation, and (2) baryon fractions ( $f_{b,200}$ ) that agree better with the mean cosmic value. While the standard AC prescriptions yield a BCG stellar mass that is uncomfortably small compared to results from stellar population synthesis (SPS) models, a weaker AC variant that artificially shuts off cooling and star formation at  $z = 2$  yields the same stellar mass as the un-contracted models. For these reasons, we believe our X-ray analysis prefers this weaker AC variant applied to either an NFW or Einasto DM halo. Finally, the stellar mass we measure for the BCG from the hydrostatic analysis strongly favors results from SPS models with a Chabrier or Kroupa IMF over a Salpeter IMF.

## 1. INTRODUCTION

The radial profiles of dark matter (DM) halos formed within the  $\Lambda$ CDM cosmology are approximately self-similar, where the deviations from self-similarity are quantified by the relation between halo concentration ( $c$ ) and mass ( $M$ ). These deviations are small and represent a variation of  $c$  of a factor of a few over about five decades in  $M$  (e.g. Dutton & Macciò 2014, and references therein). X-ray observations of the hot plasma in massive elliptical galaxies, galaxy groups, and clusters (e.g., Buote et al. 2007; Schmidt & Allen 2007; Ettori et al. 2010) obtain power-law  $c-M$  relations with normalizations and slopes consistent with  $\Lambda$ CDM after accounting for gas processes in the cosmological simulations and observational effects like selection biases (Rasia et al. 2013). The mean and slope of the  $c-M$  relation depends on cosmological parameters ( $\sigma_8, \Omega_m, w$ ; e.g., Eke et al. 2001; Alam et al. 2002; Dolag et al. 2005; Kuhlen et al. 2005; Buote et al. 2007; Macciò et al. 2008), while the scatter about the relation is the same for different variants of  $\Lambda$ CDM and is independent of halo mass (e.g. Bullock et al. 2001; Macciò et al. 2008; Dutton & Macciò 2014, and references therein). Given the robust nature of the scatter, individual outliers in the  $c-M$  relation can provide valuable tests of the general  $\Lambda$ CDM galaxy formation paradigm.

Halos classified as “fossil groups” are promising locations to search for such outliers. Fossil groups were originally conceived to be the end states of group formation (Ponman et al. 1994) where all the large galaxies merged via dynamical friction into a single large central galaxy (BCG). The entire

merger history of the group was then contained within the BCG itself, and so the “group” could then be identified with the BCG. The longer cooling time of the hot gas means the BCG is surrounded by a luminous X-ray halo characteristic of a group-scale DM halo. As such, these “classical” fossil groups were presumed to be ancient, highly relaxed, and evolved systems.

A considerable amount of work has been done over the past 10+ years characterizing the properties of fossil groups. The conception of a fossil now is broader than when initially discovered by Ponman et al. (1994) and includes more massive clusters; i.e., a fossil system is now typically defined as (at least) a 2 magnitude gap ( $R$ -band) between the BCG and next brightest member and possessing a bolometric  $L_x \gtrsim 5 \times 10^{41} \text{ erg s}^{-1}$  (e.g., Harrison et al. 2012). While cosmological simulations predict that the magnitude-gap criterion should reflect older-than-average systems (e.g., D’Onghia et al. 2005; Dariush et al. 2007; Raouf et al. 2016), the optical and X-ray properties of fossil systems are generally consistent with those of the general cluster population (e.g., Girardi et al. 2014; Kundert et al. 2015). Moreover, while it might be expected that such older systems are more dynamically relaxed, there is no evidence that the dynamical state of the hot gas in fossils is different from other clusters (Girardi et al. 2014).

If fossil systems truly formed earlier than the general population, they should possess systematically higher halo concentrations. For the NFW profile (Navarro et al. 1997), which is the standard function employed to parameterize  $\Lambda$ CDM DM

halos, the concentration is defined as,  $c \equiv r_{\Delta}/r_s$ , where  $r_s$  is the scale radius and  $r_{\Delta}$  is the radius within which the mean density is  $\Delta\rho_c$ , with  $\rho_c$  the critical density of the universe at the redshift of the halo and typically  $\Delta = 200$ . Navarro et al. (1997) argued that  $c$  is set by the mean density of the universe at the redshift of halo formation, so that halos with higher concentrations formed earlier than halos with lower concentrations. Prescriptions have been developed to associate a formation time for a given  $c$  and  $M$  (e.g., Zhao et al. 2009).

Using a modest *Chandra* ACIS-S observation for the nearby fossil group NGC 6482, Khosroshahi et al. (2004) presented intriguing evidence for an extremely high concentration value ( $c_{200} \sim 60$ ,  $M_{200} \sim 4 \times 10^{12} M_{\odot}$ ) compared to the mean  $\Lambda$ CDM  $c$ – $M$  relation ( $c \sim 7$ , e.g., Dutton & Macciò 2014), from which they inferred a very early formation time ( $z \gtrsim 5$ ). Mamon & Lokas (2005) suggested that since Khosroshahi et al. (2004) did not include a separate component for the stellar mass of the BCG in their hydrostatic equilibrium analysis, the concentration they measured was likely overestimated. Indeed, when including the stellar mass in our analysis of the *Chandra* data, we obtained a much smaller, though very uncertain, value for  $c_{200}$  that was dependent on assumptions about the baryon fraction profile (Humphrey et al. 2006, hereafter H06).

A proper interpretation of the measured halo concentration must also account for the halo response to baryons during galaxy formation. The key process leading to the steepening of the inner DM halo mass profile is “Adiabatic Contraction” (AC, Blumenthal et al. 1986), where the baryons dissipate rapidly onto the central galaxy, but the DM evolves more slowly. In particular, a discrepancy between the halo concentration as given by the mean  $c$ – $M$  relation deduced from cosmological simulations that include only DM (e.g., Dutton & Macciò 2014) with the  $c$  measured from observations using the standard NFW profile, in principle can be mitigated if instead the observations are interpreted with an adiabatically contracted NFW profile.

There are only a few applications of AC models to hydrostatic equilibrium studies of the hot X-ray-emitting gas in massive elliptical galaxies, groups, and clusters. H06 and Gastaldello et al. (2007) fitted the modified AC model of Gnedin et al. (2004) to a total of 22 massive elliptical galaxies and group-scale systems. Both of these studies found the AC model to be modestly disfavored compared to the pure NFW profile, since the AC model tended to yield BCG stellar mass-to-light ratios uncomfortably small compared to stellar population synthesis estimates. AC model fits to the hot gas of the group/cluster RXCJ2315.7-0222 by Démoclès et al. (2010) are compatible with the data but are not clearly favored over the pure NFW profile because of degeneracies in the assumed stellar initial mass function (IMF). AC models are clearly excluded by the X-ray data of the galaxy cluster A2589 (Zappacosta et al. 2006). A similar lack of evidence supporting AC occurs from lensing and stellar dynamical studies. While initially several studies found AC models to be favored (e.g., Jiang & Kochanek 2007; Grillo 2012; Sonnenfeld et al. 2012), the emerging consensus (Dutton & Treu 2014; Newman et al. 2015) is that for massive elliptical galaxies and clusters the data favor the pure NFW profile or AC that is substantially weaker than the standard prescriptions of Blumenthal et al. (1986) and Gnedin et al. (2004).

For our present investigation we revisit the halo concentra-

tion of NGC 6482 for which previous X-ray studies suggested a possibly very high, but uncertain, value. In 2010 *Suzaku* observed NGC 6482 providing the opportunity to map the hot gas to larger radius than previously and thus allow for an improved measurement of the global halo mass profile. In addition, improvements to the accuracy of the plasma code and our method of hydrostatic analysis since our study in H06 warrant a re-analysis of the *Chandra* data. Finally, we take this opportunity to investigate several variants of AC models including those with contraction weaker than the standard approaches.

We list several properties of NGC 6482 in Table 1. NGC 6482 is well-studied at multiple wavelengths and all indications are that it is an extremely relaxed object; e.g., despite the fact that the nucleus is a LINER, there is no evidence in the X-ray image or spectra for AGN emission or cavities (e.g., González-Martín et al. 2009; Panagoulia et al. 2014; Shin et al. 2016). It is also the most relaxed object in the morphological study of a sample of local X-ray galaxies (Diehl & Statler 2008). The combination of highly relaxed, evolved state and X-ray brightness make NGC 6482 an optimal low-mass group for hydrostatic equilibrium studies of its hot gas and mass profile.

The paper is organized as follows. We describe the data reduction in §2 and spectral analysis in §3. In §4 and §5 we summarize the entropy-based hydrostatic equilibrium method and the specific parameterized models. The results and the systematic error budget are discussed in, respectively, §6 and §7. We discuss many implications of our results in §8 and provide conclusions in §9. Throughout the paper we assume a flat  $\Lambda$ CDM cosmology with  $\Omega_{m,0} = 0.3$  and  $H_0 = 70 \text{ km s}^{-1} \text{ Mpc}^{-1}$ .

## 2. OBSERVATIONS AND DATA PREPARATION

Table 2 lists details of the *Chandra* and *Suzaku* observations of NGC 6482. Below we describe how the data were prepared for spectral analysis (§3). We defer discussion of possible Solar Wind Charge Exchange (SWCX) emission to §7.5.

### 2.1. *Chandra*

*Chandra* observed NGC 6482 on-axis with the ACIS instrument in the ACIS-S configuration for  $\approx 20$  ks in 2002 as part of observing cycle AO3. We prepared the data for spatially resolved spectral analysis using the CIAO (v4.8) and HEASOFT (v6.18) software suites along with version 4.7.1 of the *Chandra* calibration database. First, we followed the standard *Chandra* data-reduction threads<sup>1</sup> and reprocessed the level 1 events file using the latest calibration. Next, we extracted a light curve from regions free of obvious point sources and the main emission of NGC 6482. From visual inspection of the light curve we removed periods of high background which resulted in the exclusion of  $\approx 2$  ks giving a final, cleaned exposure of 17.5 ks. From the cleaned events list we constructed an image in the 0.3–7.0 keV band to detect point sources using the CIAO WAVDETECT tool. We set the detection threshold to  $10^{-6}$  and used a 1.7 keV monochromatic exposure map. All point sources detected by WAVDETECT were verified by eye.

We extracted spectra in a series of concentric, circular annuli positioned at the optical center of the elliptical galaxy (Fig. 1). Point sources, chip gaps, and any off-chip regions were masked out. We adjusted the widths of the annuli so that each annulus contained  $\approx 1000$  background-subtracted counts, which resulted in 9 annuli within a radius of  $184.5'' (3.1')$ . These annuli are located entirely on the

<sup>1</sup> <http://cxc.harvard.edu/ciao/threads/index.html>

**Table 1**  
Target Properties

Name	Redshift	Distance (Mpc)	$N_{\mathrm{H}}$ ( $10^{20} \text{ cm}^{-2}$ )	$L_{\mathrm{K}}$ ( $10^{11} L_{\odot}$ )	$R_e$ (kpc)	$L_{\mathrm{x},500}$ ( $10^{41} \text{ ergs s}^{-1}$ )
NGC 6482	0.013129	59.2	7.7	3.3	$3.65 \pm 0.85$	$5.0 \pm 0.3$

**Note.** — The redshift is taken from NED<sup>a</sup>. For the distance we use the radial velocity corrected for Local Group infall onto Virgo from LEDA<sup>b</sup>. (The angular scale is  $1'' = 0.279 \text{ kpc}$ .) We calculate the Galactic column density using the HEASARC W3NH tool based on the data of Kalberla et al. (2005). The  $K$ -band luminosity is from 2MASS while the effective radius ( $R_e$ ) represents an average of the 2MASS value and that obtained after applying a correction (see §5.2).  $L_{\mathrm{x},500}$  is the 0.1-10.0 keV luminosity computed for the fiducial hydrostatic model within a three-dimensional volume with radius  $r_{500}$  (§6).

<sup>a</sup><http://ned.ipac.caltech.edu>

<sup>b</sup><http://leda.univ-lyon1.fr/>

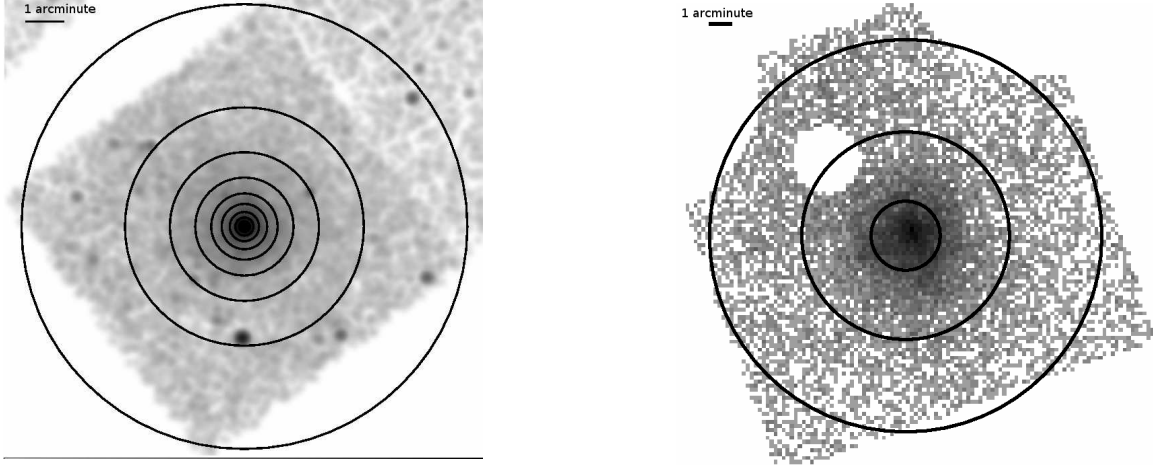


**Figure 1.** Regions adopted for spectral analysis. (Left Panel) *Chandra* spectral extraction regions overlaid on the raw image (without point sources masked out). The outermost annulus (i.e., Annulus 11) used only for background modeling is not shown. (Right Panel) *Suzaku* spectral extraction apertures overlaid on the processed XIS1 image with sources (point and calibration) masked out.

**Table 2**  
Observations

Telescope	Obs. ID	Obs. Date	Instrument	Exposure (ks)
<i>Chandra</i>	3218	2002, May 20	ACIS-S	17.5
<i>Suzaku</i>	804050010	2010, Feb. 11	XIS	43.4

**Note.** — The exposure times refer to those obtained after filtering the light curves (§2). The exposures for the *Chandra* and *Suzaku* observations before filtering were 19.6 ks and 43.7 ks respectively.

ACIS-S3 CCD. We also included two additional annuli (Annulus 10:  $3.1' - 5.7'$ , Annulus 11:  $5.7' - 12.3'$ ), with smaller numbers of source counts to facilitate simultaneous determination of the background. Annulus 10 is located mostly on the S3 chip, but with its outermost regions largely off any active ACIS CCD except for some parts that fall on the S2. (This is the largest annulus shown in Fig. 1.) Annulus 11 (not shown) partly overlaps the active CCDs S2, I2, and I3.

For each annulus we constructed counts-weighted response files (ARFs and RMFs) using the CIAO tools MKWARF and MKACISRMF. In Fig. 2 we plot representative spectra. Note that we do not subtract any background beforehand. Instead, we model it and fit it simultaneously with the hot gas emission below (§3). For all spectral fitting with *Chandra* we include only data between 0.5-7.0 keV.

## 2.2. *Suzaku*

As part of observing cycle AO4, in 2010 *Suzaku* observed NGC 6482 with the XIS instrument for a nominal exposure of 46.5 ks at a location slightly offset ( $\approx 0.9'$ ) from the optical position. We prepared the data for spatially resolved spectral analysis using the HEASOFT (v6.18) software suite along with version 20160204 of the *Suzaku* calibration database. We followed the standard *Suzaku* data-reduction threads<sup>2</sup> and used the AEPIPELINE tool to reprocess the events using the latest calibration. Data taken in  $5 \times 5$  readout mode were converted to  $3 \times 3$  mode and then were merged with the original  $3 \times 3$  mode data. We also applied an additional screening on geomagnetic cutoff rigidity (i.e.,  $\text{COR2} > 6$ ) to reduce the particle background as recommended in the standard data-reduction threads. We visually inspected the light curve to remove any periods of high background. Since the observation was very quiescent, only about 0.3 ks were removed resulting in a cleaned exposure of 43.4 ks. We masked out regions near the calibration sources and surrounding one faint point source located  $\sim 5'$  to the NE of NGC 6482. For the point source we used a circular region of radius  $1.5'$ . While this radius encloses only  $\sim 70\%$  of the point source counts, larger regions would unacceptably exclude more diffuse emission of NGC 6482.

We extracted spectra for the XIS0, XIS1, and XIS3 in three

<sup>2</sup> <http://heasarc.gsfc.nasa.gov/docs/suzaku/analysis/abc/>

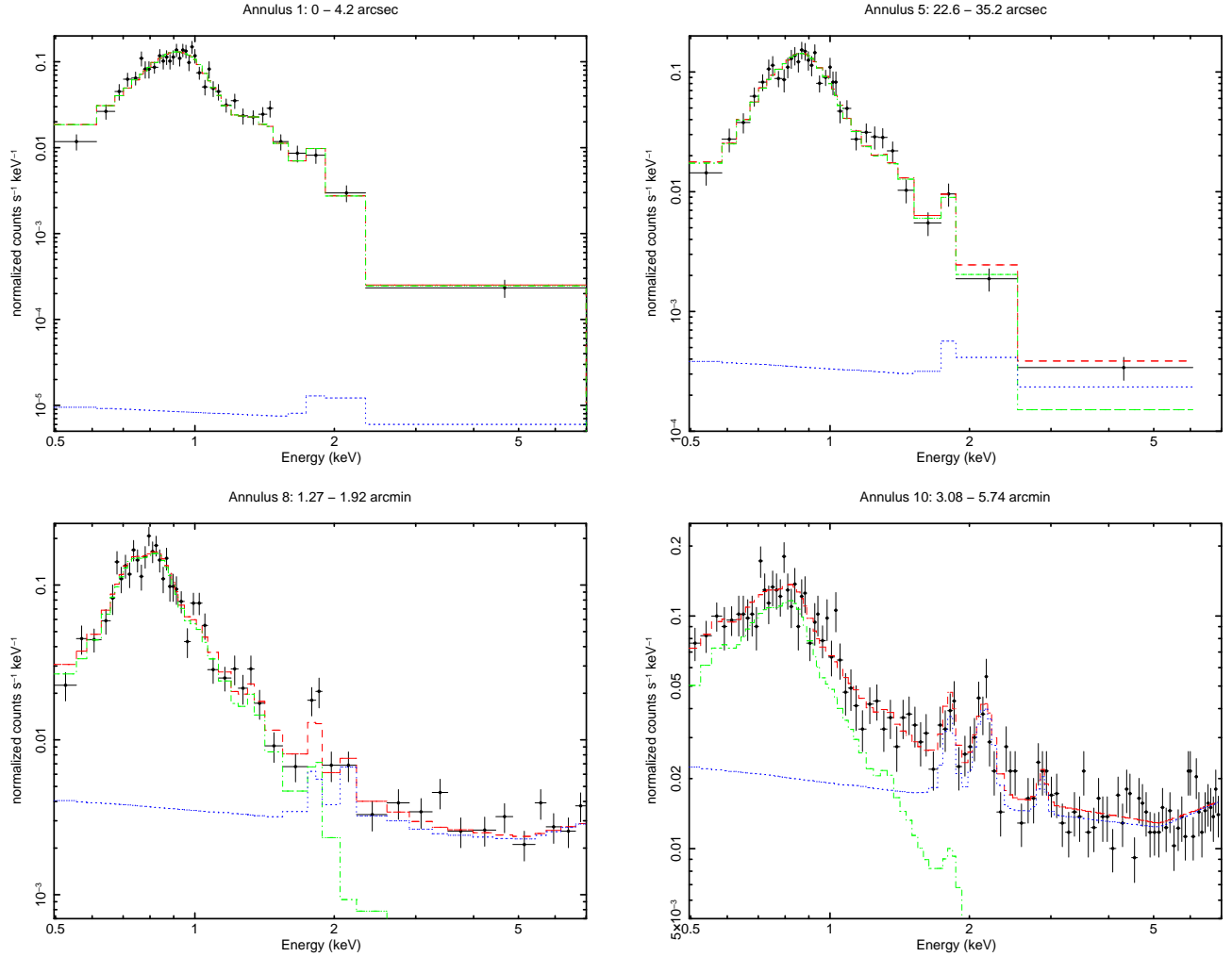


**Figure 2.** Representative *Chandra* spectra in the 0.5-7.0 keV band without any background subtraction. Also plotted are the best-fitting models (red dashed) broken down into the separate contributions from the following: (1) hot gas and unresolved LMXBs from NGC 6482 along with the CXB (green dot-dash), and (2) particle background (blue dotted).

concentric annuli ( $0' - 1.5'$ ,  $1.5' - 4.5'$ ,  $4.5' - 8.5'$ ) centered on NGC 6482 (Fig. 1). For each spectrum we created an associated RMF file using the task `XISRMFGEN`. Unlike with *Chandra*, it is necessary to account for spatial mixing between different annuli because of the large point spread function of *Suzaku* ( $\sim 2'$  HPD). Consequently, we created special mixing ARF files following Humphrey et al. (2011) using the task `XISSIMARFGEN` (Ishisaki et al. 2007). Since the `XISSIMARFGEN` task, which performs ray-tracing calculations, requires a model image for the true spatial source profile, we constructed one from the *Chandra* image using two  $\beta$  models with the same  $\beta$  for each component. The parameters were obtained by fitting the 0.5-7.0 keV *Chandra* surface brightness profile in conjunction with appropriate background terms. We found the model to be a good fit with best-fitting parameters,  $\beta = 0.57$ ,  $r_{c,1} = 3.8''$ ,  $r_{c,2} = 29''$ , and relative normalization of component 2 to 1 of 0.99. Finally, for each spectrum we also generated corresponding Non-X-ray (i.e., particle) Background (NXB) spectral files using the task `XISNXBGEN`.

For the spectral fitting below in §3, we initially considered data between 0.5-7.0 keV for all detectors like we did with *Chandra*. From visual inspection of the spectra and comparison to the spectral models, we decided to restrict further the fitted energy ranges of the *Suzaku* data. The data at high en-

ergies contain little contribution from NGC 6482 and are instead dominated by the NXB and CXB. To reduce any sensitivity of our results on the accuracy of the NXB model we lowered the upper bandpass limit from 7.0 to 5.25 keV. As for the lower energy limit, we noticed that the two front-illuminated (FI) CCDs (XIS0, XIS3) generally exhibited large fit residuals near the lower bandpass limit. Consequently, we excluded energies below 0.7 keV for the FI CDDs. Therefore, we used the following energy ranges in the spectral fitting: XIS0, XIS3: 0.7-5.25 keV, XIS1: 0.5-5.25 keV.

We plot the XIS1 spectra of Annulus 2 and Annulus 3 in Figure 3.

### 3. SPECTRAL ANALYSIS

We fitted models to the spectra in a standard frequentist approach using `XSPEC v12.9.0k` (Arnaud 1996) by minimizing the C-statistic (Cash 1979) to mitigate biases associated with the  $\chi^2$  statistic for Poisson-distributed data even in the high-counts regime (Humphrey et al. 2009b). While not strictly necessary when using the C-statistic, we rebinned each spectrum so that each data bin contained a minimum of 20 counts. Humphrey et al. (2009b) note that, like with the  $\chi^2$  statistic, rebinning the data can improve model selection by emphasizing differences between the model and data. In addition,

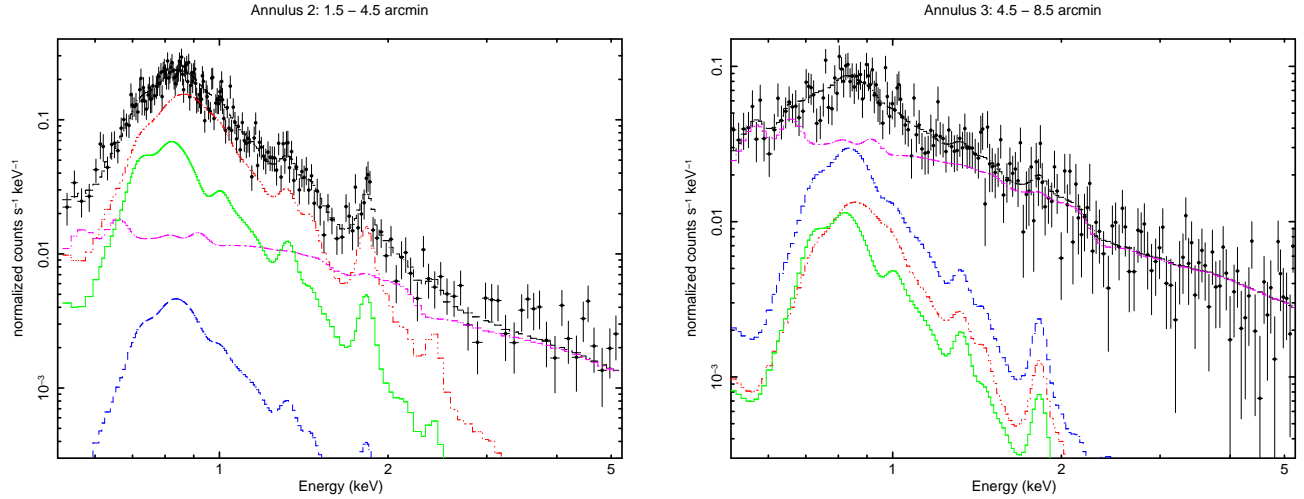


**Figure 3.** *Suzaku* spectra in the 0.5-7.0 keV band with the NXB subtracted for annulus 2 (Left Panel) and annulus 3 (Right Panel). Also plotted are the best-fitting models (black solid) broken down into the separate contributions from the following: hot gas from NGC 6482 from annulus 1 (green solid), annulus 2 (red dot-dash), and annulus 3 (blue dash) along with CXB (magenta dash). Notice in particular that hot gas emission is clearly visible near  $\lesssim 1$  keV in both annuli.

**Table 3**  
Hot Gas Properties

Telescope	Annulus	$R_{\text{in}}$ (kpc)	$R_{\text{out}}$ (kpc)	$\Sigma_{\text{x}}$ (0.5-7.0 keV) (ergs cm <sup>2</sup> s <sup>-1</sup> arcmin <sup>-2</sup> )	$k_{\text{B}}T$ (keV)	$Z_{\text{Fe}}$ (solar)
<i>Chandra</i>						
	1	0.00	1.17	$1.83\text{e-}11 \pm 3.21\text{e-}12$	$0.958 \pm 0.019$	$0.68 \pm 0.16$
	2	1.17	2.34	$5.94\text{e-}12 \pm 1.13\text{e-}12$	$0.889 \pm 0.021$	$1.06 \pm 0.24$
	3	2.34	3.92	$2.49\text{e-}12 \pm 4.53\text{e-}13$	$0.830 \pm 0.018$	tied
	4	3.92	6.32	$9.40\text{e-}13 \pm 1.38\text{e-}13$	$0.828 \pm 0.018$	$0.67 \pm 0.10$
	5	6.32	9.83	$3.99\text{e-}13 \pm 5.78\text{e-}14$	$0.801 \pm 0.019$	tied
	6	9.83	14.36	$1.97\text{e-}13 \pm 3.14\text{e-}14$	$0.711 \pm 0.019$	$0.66 \pm 0.13$
	7	14.36	21.23	$9.16\text{e-}14 \pm 1.51\text{e-}14$	$0.621 \pm 0.017$	tied
	8	21.23	32.16	$3.78\text{e-}14 \pm 6.44\text{e-}15$	$0.575 \pm 0.017$	tied
	9	32.16	51.53	$1.42\text{e-}14 \pm 4.05\text{e-}15$	$0.578 \pm 0.024$	$0.26 \pm 0.08$
	10	51.53	96.19	$5.45\text{e-}15 \pm 8.77\text{e-}16$	$0.588 \pm 0.035$	tied
<i>Suzaku</i>						
	2	25.14	75.42	$8.20\text{e-}15 \pm 3.78\text{e-}15$	$0.572 \pm 0.042$	$0.58 \pm 0.43$
	3	75.42	142.45	$1.44\text{e-}15 \pm 7.64\text{e-}16$	$0.647 \pm 0.072$	tied

**Note.** — 1 kpc = 3.58". Annuli where the iron abundance is linked to the value in the previous annulus are indicated as "tied." See §3.3 for discussion of the central *Suzaku* annulus.

fewer bins typically translates to fewer model evaluations and therefore speedier convergence. In §7.7 we compare results using the C-statistic to those obtained using standard  $\chi^2$ .

Unless stated otherwise, all quoted parameter errors represent 68% confidence limits on one interesting parameter obtained using the ERROR command in XSPEC. For the C-statistic this standard procedure begins with the model evaluated with the best-fitting values of all the parameters. Then the parameter of interest is stepped to lower and higher values (while all other free parameters are varied to minimize C) until the C-statistic increases by 1 from its best-fitting value.

### 3.1. Spectral Models

The procedure we adopt to interpret the X-ray spectra closely follows that used originally for *XMM-Newton* data of the galaxy group NGC 5044 (Buote et al. 2004) and has been refined modestly in subsequent studies, the most re-

cent of which (Su et al. 2015) examined a combination of *Chandra* and *Suzaku* as in our present study. Here we summarize the models that we fitted separately to the *Chandra* and *Suzaku* spectral data. Unless stated otherwise, all the emission models described below were modified by foreground Galactic absorption with the PHABS model in XSPEC using the photoelectric absorption cross sections of Balucinska-Church & McCammon (1992) and a hydrogen column density,  $N_{\text{H}} = 7.7 \times 10^{20} \text{ cm}^{-2}$  (Kalberla et al. 2005).

#### 3.1.1. Galactic Emission Models

The principal source of X-ray emission from NGC 6482 is the hot, diffuse interstellar medium (ISM) / intragroup medium (IGrM). We account for this emission with the VAPEC coronal plasma model in XSPEC. We do not perform onion-peeling-type deprojection (e.g., using the PROJCT mixing model in XSPEC) because it amplifies noise particularly

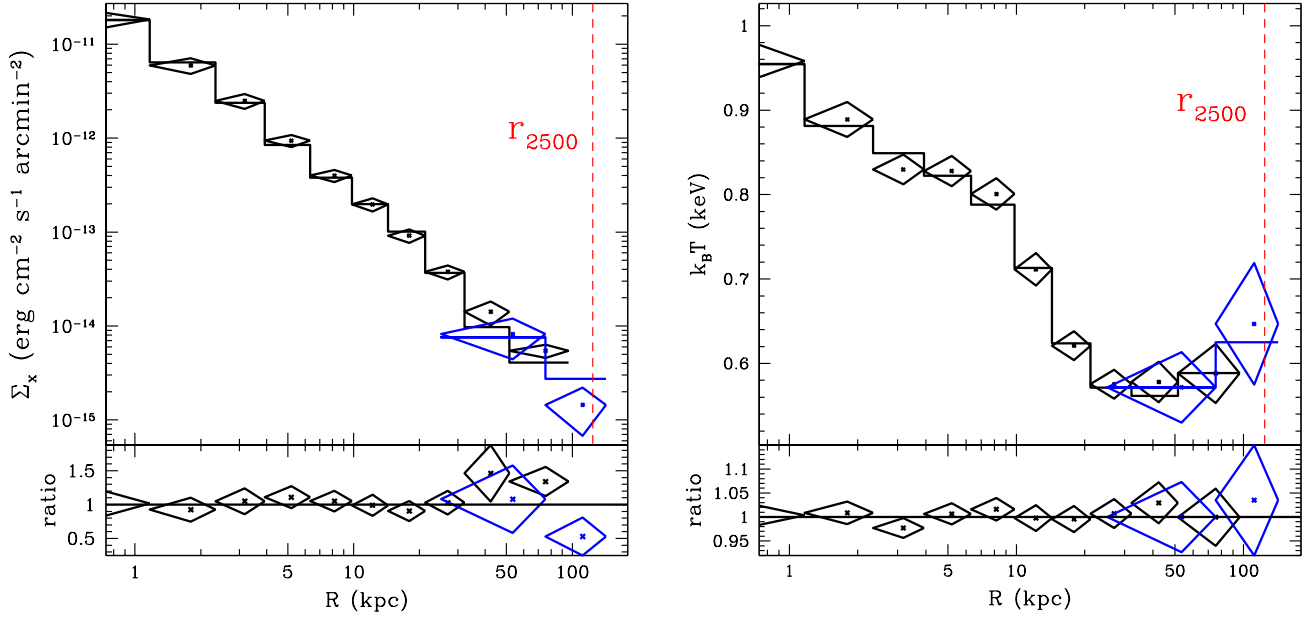


**Figure 4.** *Chandra* (black) and *Suzaku* (blue) data,  $1\sigma$  errors, and the best-fitting fiducial hydrostatic model in each circular annulus on the sky. (Left Panel) Surface brightness (0.5–7.0 keV). (Right Panel) Projected emission-weighted temperature ( $k_B T$ ). The bottom panels plot the data/model ratios.

in the challenging background-dominated outer regions. In addition, the ISM emission outside the bounding annulus is not easily accounted for by the standard deprojection algorithms, which can be a sizable source of systematic error (e.g., Nulsen & Bohringer 1995; McLaughlin 1999; Buote 2000a).

As is readily apparent from Figures 2 and 3, the broad “hump” near 1 keV composed of an unresolved forest of emission lines from iron L-shell transitions is the dominant spectral line feature. After iron, for  $k_B T \sim 1$  keV the strongest line features arise from K-shell transitions of O, Ne, Mg, Si, and S. For both *Chandra* and *Suzaku*, the O, Ne, and Mg lines are heavily blended with the strong, highly temperature-sensitive Fe-L lines. Consequently, in our spectral model these weaker, unresolved lines may attempt to partially compensate for inaccuracies in the Fe-L lines due to, e.g., plasma code deficiencies or the assumed temperature structure that gives rise to the Fe Bias (Buote 2000b; see also Buote & Canizares 1994; Buote & Fabian 1998; Buote 1999, 2000a; Molendi & Gastaldello 2001; Buote et al. 2003b); i.e., the underestimate of the iron abundance when assuming a single plasma temperature when in fact multiple temperature components are present arising from, e.g., a range of temperatures due to the projection along the line of sight of a radial temperature gradient. The Si and S lines do not suffer from blending with the Fe L shell lines, but they are contaminated by strong lines in the particle background. Therefore, by default we assume a single temperature component for each spectrum and allow the iron abundance to be fitted freely while restricting the other metal abundances to vary in their solar ratios with respect to iron; e.g., for silicon, the quantity  $Z_{\text{Si}}/Z_{\text{Fe}}$  is fixed at the solar ratio. For completeness, however, we also examine the effects of allowing the non-Fe abundances to be varied separately and adding additional temperature components. By default we employ the solar abundance standard of Asplund et al. (2006).

A weaker source of emission arises from unresolved discrete sources in the galaxy, especially from Low-Mass X-Ray

binaries (LMXBs). We represent the spectrum of these unresolved point sources by a thermal bremsstrahlung component with  $k_B T = 7.3$  keV and assume it follows the stellar mass by requiring the relative fluxes in the different annuli to obey the K-band light profile (§5.2). We only include this model interior to  $D_{25}$  (i.e.,  $\lesssim 1'$ ) which corresponds to annuli 1–6 for *Chandra* and the inner annulus ( $< 1.5'$ ) for *Suzaku*. Based on the K-band luminosity, the expected 0.3–7.0 keV luminosity within  $D_{25}$  from the LMXBs is,  $L_{\text{LMXB}} = (3.5 \pm 2.1) \times 10^{40}$  erg s $^{-1}$ , using the scaling relation of Humphrey & Buote (2008, i.e., their equation 8).

For the *Suzaku* data we obtain a fitted value consistent with the scaling relation. For the *Chandra* data our best-fitting value is  $L_{\text{LMXB}} \approx 5.0 \times 10^{40}$  erg s $^{-1}$ ; i.e., about  $1\sigma$  above the predicted value. Given the nature of our complex, multi-component spectral model with source and background emission, the LMXB component is somewhat degenerate with the CXB and particle background models, which likely accounts for the possible discrepancy. Consequently, by default for the *Chandra* spectral fitting we fixed  $L_{\text{LMXB}}$  at the predicted value from the scaling relation and treated as a systematic error the case where  $L_{\text{LMXB}}$  is allowed to be freely fitted (§7.7).

### 3.1.2. Background Emission Models

We account for the cosmic X-ray background (CXB) with several model components. The soft portion of the CXB consists of emission from the Local Hot Bubble (LHB) and hot plasma associated with the disk and halo of the Milky Way (e.g., Kuntz & Snowden 2000). Since the temperatures associated with these components ( $k_B T \approx 0.1$ – $0.2$  keV) are well below the band-pass of our observations, we find that at most two separate soft components are needed, as in, e.g., Lumb et al. (2002). As we did in Su et al. (2015), we include separate components for the LHB (unabsorbed APEC component with  $k_B T = 0.08$  keV and solar abundances) and the halo gas (absorbed APEC component with  $k_B T = 0.20$  keV and solar abundances). The hard portion of the CXB is dominated



by unresolved AGN which we model as a power-law with index  $\Gamma = 1.41$  (e.g., De Luca & Molendi 2004).

As mentioned above in §2.2, we adopt a standard model for the particle background and subtract it from the *Suzaku* spectra before fitting. For *Chandra*, however, we parameterize the particle background with a simple broken power-law model and several Gaussian components – none of which are folded through the ARF (i.e., the particle background model components are “un-vignetted”) – which we find is sufficient to provide an acceptable description of the data. In particular, to obtain a good fit for the particle background for annuli 1-10 (which lie mostly on the BI chip S3) we added three gaussian components with best-fitting central energies, 1.81, 2.17, and 2.88 keV. Their emission is easily seen in the spectrum of annulus 10 shown in Figure 2. For annulus 11, which spans three FI chips, the most important gaussian component we added has energy 2.17 keV, though we also added minor components at 1.49 keV and 2.51 keV.

We required the CXB to be uniform across the field. Therefore, we tied all CXB parameters for all annuli and insured that the fluxes of the CXB model components were the same in each annuli when rescaled to the aperture area. The same was done for the *Chandra* particle background model. We experimented with allowing the particle background normalizations to vary separately for each annulus and found the results were not changed significantly.

### 3.2. *Chandra*

In addition to background and LMXB components, the fiducial spectral model described above (§3.1) consists of a single VAPEC coronal plasma component for each annulus where only the temperature, normalization, and iron abundance (all other elements tied to iron in their solar ratios) are allowed to vary. We find this fiducial model provides a good overall fit to the data with a minimum C-statistic of 631.85 for 595 degrees of freedom (dof). This best fit also translates to a reduced  $\chi^2 = 1.07$  with a null hypothesis probability of 12%, indicating a formally acceptable fit. The good quality of the global fit is on display in Figure 2 where we show the best-fitting model over-plotted on the spectra in four of the annular regions.

For the hot gas we list the surface brightness ( $\Sigma_x$ ), temperature ( $k_B T$ ), and  $Z_{Fe}$  for each annulus in Table 3 and plot the radial profiles of  $\Sigma_x$  and  $k_B T$  in Figure 4. We define  $\Sigma_x$  to be the 0.5-7.0 keV flux ( $\text{erg cm}^2 \text{s}^{-1}$ ) of the gas emission in the aperture divided by the aperture solid angle taken to be  $\pi\theta^2$  ( $\text{arcmin}^2$ ). The temperature profile peaks at the center ( $k_B T \approx 0.96$  keV) and decreases with radius until flattening out in the last two bins (9-10) with a slight hint of an upturn that is more pronounced in the *Suzaku* spectra (§3.3).

The shape of the declining temperature profile agrees well with our previous study of NGC 6482 by H06 using similar models and data reduction methods. However, the temperatures we have measured here systematically exceed those reported by H06 by  $\approx 20\%$ , while our iron abundances are much smaller. In our present study the VAPEC plasma emission code uses the current version (2.0.2) of the atomic database ATOMDB<sup>3</sup>, whereas H06 used version 1.3.1. We find that if we force XSPEC to use ATOMDB version 1.3.1, then we obtain results that are overall very consistent with those of H06.

Even though we obtain a fit that is formally acceptable, we examined whether the fit could be improved further. Perhaps

the most notable fit residuals occur between 0.5-0.6 keV for annulus 1, and also annuli 3-4 (not shown), where the model over-predicts the data by  $\sim 60\%$  with 2-3  $\sigma$  significance. (Excluding these bins does not affect the fitted parameters much.) Other notable, but less significant, residuals occur in the Fe-L region (i.e., 0.7-1.4 keV) at approximately the  $\pm 25\%$  level for annuli 1-6. These features are characteristic of the Fe Bias (§3.1.1), but since the annular widths are fairly small, the effect is not highly significant; for a more detailed study of the effect of aperture width on the Fe Bias, see, e.g., the case of NGC 5044 (Buote et al. 2003a,b). Indeed, we find that adding a second temperature component leads to only a marginal improvement in the fit while leading to much more poorly constrained gas parameters.

We also find that essentially the same reduction in the C-statistic obtained by adding a second temperature component can be achieved instead by allowing some other elemental abundances to be varied separately from iron. Since the abundances of these other elements are not as well constrained as iron, we tied their values for all annuli. When doing so, the largest fit improvement occurs for Ne, Mg and Si respectively for which we obtain the following abundance ratios (in solar units):  $Z_{Ne}/Z_{Fe} = 2.5^{+0.4}_{-0.3}$ ,  $Z_{Mg}/Z_{Fe} = 1.6 \pm 0.1$ , and  $Z_{Si}/Z_{Fe} = 1.3^{+0.4}_{-0.3}$ . Since we expect that these non-solar abundance ratios reflect to a large extent the Fe Bias, we treat this variable abundance case as a systematic error for the mass models (§7.7).

### 3.3. *Suzaku*

The *Suzaku* data from all annuli and all instruments (XIS0, XIS1, XIS3) are fitted simultaneously. To account for any relative calibration uncertainties between the detectors, we allow the relative normalizations of the model components for the XIS1 and XIS3 to vary with respect to the XIS0 through the use of additional multiplicative constants.

The strong temperature gradient measured by *Chandra* within the region of annulus 1 (i.e.,  $< 1.5'$ , see Table 3) compels us to consider multiple temperatures there so that the spatial mixing between annuli due to the large PSF is sufficiently accurate in our model for all annuli. Like our previous study of RXJ 1159+5531 (Humphrey et al. 2012a; Su et al. 2015), for this purpose we adopted a simple two-temperature model (2T), since we have shown previously that such a simple model provides a good description at CCD resolution of the integrated spectrum in a region containing a radial temperature gradient (Buote 1999; Buote et al. 2003a). The 2T model improves the global fit modestly (i.e.,  $\Delta C = 11.0$ ,  $\Delta\chi^2 = 12.6$  for 1136 dof and 3 additional parameters), so that the gas parameters in the other annuli are also modestly affected. For example, in annulus 2,  $k_B T$  rises from 0.47 keV (1T) to 0.57 keV (2T), the difference of which is  $\approx 2.5\sigma$  significant. We therefore employ the 2T model in annulus 1 (and 1T models in annuli 2 and 3) for the fiducial model of the *Suzaku* spectra and treat the case of using the 1T model in annulus 1 as a systematic error (§7.7).

Whereas we obtain tight constraints on the gas parameters in annulus 1 for a 1T model (e.g.,  $k_B T = 0.766 \pm 0.006$  keV,  $Z_{Fe} = 0.70 \pm 0.08 Z_{\odot}$ ), for the 2T model the temperatures for each component are not very well constrained. In fact, the emission-weighted parameters of the 2T model (e.g.,  $k_B T = 0.73 \pm 0.12$  keV) have much larger uncertainties than the corresponding *Chandra* measurements in the same region. Consequently, we find that annulus 1 does not provide tangible

<sup>3</sup> <http://www.atomdb.org>

constraining power for the hydrostatic models (§5) above that provided by the *Chandra* data, and thus we do not include annulus 1 in our subsequent analysis.

From visual inspection of Figure 3, where we show the best-fitting fiducial model to the spectra in annuli 2-3, it is apparent that the fiducial model provides a good description of the data there, and the strong spatial mixing of the gas components is readily seen. The best fit yields a C-statistic of 1349.35 for 1136 dof and reduced  $\chi^2 = 1.20$ . Unlike the *Chandra* data, the *Suzaku* fit is not formally acceptable, and we were unable to greatly improve the fit with small alterations to the fiducial model (e.g., varying other abundances, see below). The most prominent model residuals occur for annulus 1 (not shown), providing additional justification for not including the parameters of annulus 1 in our subsequent analysis.

We list the parameters for the hot gas for annuli 2-3 in Table 3 and plot them in Figure 4. The parameters of annulus 2 measured by *Suzaku* agree very well with those measured by *Chandra* in their overlapping region (i.e., *Chandra* annuli 8-10) but with larger statistical error. For annulus 3, which is mostly exterior to the *Chandra* data, the temperature appears to rise. Though the rise is not very significant ( $\sim 1\sigma$ ), it is consistent with the hint of a rise in *Chandra* annuli 8-10. The isolated elliptical galaxy NGC 1521 (Humphrey et al. 2012b), which has a halo mass similar to NGC 6482, displays a similar rise in temperature near  $r_{2500}$ .

Allowing the Ne abundance to be free yields a super-solar value ( $Z_{\text{Ne}}/Z_{\text{Fe}} = 2.2 \pm 0.3$ ) very consistent with that obtained from *Chandra* (§3.2). However, for Mg and Si we obtain ratios,  $Z_{\text{Mg}}/Z_{\text{Fe}} = 1.09 \pm 0.08$ , and  $Z_{\text{Si}}/Z_{\text{Fe}} = 1.00 \pm 0.07$ , very consistent with solar and, particularly for Mg, significantly less than obtained with *Chandra*. As we do for *Chandra*, we treat this variable abundance case as a systematic error for the mass models (§7.7).

#### 4. ENTROPY-BASED METHOD

To measure the mass profile from the X-ray observations we adopt the entropy-based approach of Humphrey et al. (2008); see Buote & Humphrey (2012a) for a discussion of the benefits of this approach and a review of other hydrostatic methods. The equation of hydrostatic equilibrium may be written in terms of the variable  $\xi \equiv P^{2/5}$ , with  $P$  the total thermal pressure, so that

$$\frac{d\xi}{dr} = -\frac{2}{5} \frac{GM(<r)}{r^2} S_\rho^{-3/5}, \quad (1)$$

where  $M(<r)$  is the total gravitating mass enclosed within radius  $r$ , and

$$S_\rho \equiv \frac{k_B T}{\mu m_a \rho_{\text{gas}}^{2/3}} = \frac{S}{\mu m_a} \left( \frac{2+\mu}{5\mu} \frac{1}{m_a} \right)^{2/3}. \quad (2)$$

The quantity  $S \equiv k_B T n_e^{-2/3}$  is the conventional entropy proxy expressed in units of  $\text{keV cm}^2$ ,  $m_a$  is the atomic mass unit, and  $\mu$  is the mean atomic mass of the hot ISM. We take  $\mu = 0.62$  for a fully ionized cosmic plasma.

We assume parameterized functions for  $S$ , BCG stellar mass, and DM, insert them into Equation 1, and solve for  $\xi$  using an iterative procedure to ensure the gas mass is treated self-consistently (Buote et al. 2016). For the boundary condition on  $\xi$  we choose the value of the pressure at a radius of 1 kpc which we designate as the “reference pressure,”  $P_{\text{ref}}$ . Given a solution for  $\xi$  we compute profiles of

gas density,  $\rho_{\text{gas}} = (P/S_\rho)^{3/5} = S_\rho^{-3/5} \xi^{3/2}$ , and temperature,  $k_B T / \mu m_a = S_\rho^{3/5} P^{2/5} = S_\rho^{3/5} \xi$ .

We compare this hydrostatic equilibrium model to the observations as follows. Using the three-dimensional profiles of  $\rho_{\text{gas}}$  and  $k_B T$  we construct the X-ray volume emissivity,  $\epsilon_\nu \propto \rho_{\text{gas}}^2 \Lambda_\nu(T, Z)$ , where  $\Lambda_\nu(T, Z)$  is the plasma emissivity of the VAPEC model in XSPEC. We project  $\epsilon_\nu$  and the emission-weighted temperature along the line of sight using equations (64) and (67) of Buote & Humphrey (2012b) for a spherical system but with the aperture luminosity replaced by the flux and the aperture area expressed in square arcseconds (see also Appendix B of Gastaldello et al. 2007). Then we compare the resulting surface brightness  $\Sigma_x$  and projected temperature map to the observations.

To fully specify  $\Lambda_\nu(T, Z)$  also requires the radial elemental abundance profiles to be specified. In our previous studies of elliptical galaxies and galaxy clusters we have found that simply using the measured projected elemental abundance profiles for the true three-dimensional profiles for the models yields satisfactory results. In §7.8 we examine an alternative procedure to account for the metal abundance profile in the hydrostatic models.

### 5. MODELS

#### 5.1. Entropy

To represent the profile of the entropy proxy we use the simple function,

$$S(r) = s_0 + s_1 f(r), \quad (3)$$

where  $s_0$  is a spatially uniform constant,  $s_1 = S(1 \text{ kpc}) - s_0$ , and  $f(r)$  is a dimensionless function with  $r$  expressed in kpc,

$$f(r) = \begin{cases} r^{\alpha_1} & r \leq r_{b,1} \\ f_1 r^{\alpha_2} & r_{b,1} < r \leq r_{b,2} \\ f_2 r^{\alpha_3} & r > r_{b,2} \end{cases}$$

The two break radii are denoted by  $r_{b,1}$  and  $r_{b,2}$  and the coefficients  $f_1$  and  $f_2$  are,

$$f_n = f_{n-1} r_{b,n}^{\alpha_n - \alpha_{n+1}},$$

with  $f_0 \equiv 1$ . We restrict  $\alpha_1, \alpha_2, \alpha_3 \geq 0$  to enforce convective stability consistent with the condition of hydrostatic equilibrium. In addition, we ensure that beyond some radius  $r_{\text{baseline}}$  the logarithmic entropy slope matches that of the baseline entropy profile (i.e.,  $\approx 1.1$ ) derived from cosmological simulations with only gravity (e.g., Tozzi & Norman 2001; Voit et al. 2005). We find our results are not very sensitive to the choice of  $r_{\text{baseline}}$ . By default we set  $r_{\text{baseline}} = 200 \text{ kpc}$ , which lies between  $r_{2500}$  and  $r_{500}$  and is not far outside the measured data extent. We treat a larger value of  $r_{\text{baseline}}$  as a systematic error (§7.2).

#### 5.2. Stellar Mass

Since the  $K$ -band light should trace stellar mass more closely than that of shorter wavelengths, we represent the stellar mass of the BCG using the  $K$ -band light profile from the Two Micron All-Sky Survey (2MASS) as listed in the Extended Source Catalog (Jarrett et al. 2000). We convert the 2MASS total  $K$ -band magnitude ( $k_{\text{m\_ext}} = 8.372$ ) to absolute magnitude following equation (1) of Ma et al. (2014) using Galactic extinction  $A_V = 0.277$  and distance  $D = 59.2 \text{ Mpc}$  to yield,  $M_K = -25.52$  and thus  $L_K = 3.3 \times 10^{11} L_\odot$  (Table 1). Despite the relatively shallow 2MASS photometry, Ma et al.



(2014) find no evidence that the total  $K$ -band magnitudes in their local sample of elliptical galaxies have been systematically underestimated.

To assign the 2MASS effective radius to our spherical models we follow the procedure of Cappellari et al. (2011) and take the median effective semi-major axes from the  $J$ -,  $H$ -, and  $K$ -band photometry and convert it to a spherical radius using the geometric mean of the 2MASS effective minor and major axes to yield,  $R_e = 10.1'' = 2.8$  kpc. There is widespread evidence, however, that the typical effective radius obtained by the 2MASS photometry is smaller than obtained from analysis of photometry at shorter wavelengths. For example, Ma et al. (2014)’s equation (4) provides a conversion between the typical effective radius measured by 2MASS and the NASA-Sloan Atlas (NSA). Using this conversion for NGC 6482, we obtain  $R_e = 4.5$  kpc which is  $\approx 60\%$  larger than the 2MASS value. Although the  $K$ -band is preferred for representing the stellar mass, given the large differences in the effective radius just noted, we adopt for our fiducial model the mean of the 2MASS and NAS values (i.e.,  $R_e = 3.65$  kpc) and consider the full range 2.8–4.5 kpc as a systematic error (§7.3).

In our models we treat the stellar mass-to-light ratio ( $M_*/L_K$ ) of the BCG as a free parameter. To provide a check on the accuracy of our hydrostatic model as well as provide a constraint on the stellar initial mass function (IMF), it is interesting to compare  $M_*/L_K$  determined from the hydrostatic analysis to that obtained from single-burst stellar population synthesis (SPS) models. In H06 we provided SPS estimates of  $M_*/L_K$  for NGC 6482 based on updated versions of the models of Maraston (1998) and an age and metallicity derived from Lick indices. Since no uncertainty was used for the age in H06, we have updated the SSP fits using the same procedure as H06 but with 10% error on the age of NGC 6482 as found by Sánchez-Blázquez et al. (2006). For an age  $12 \pm 1.2$  Gyr and metallicity  $[Z/H] = 0.06 + / - 0.15$ , we obtain  $M_*/L_K$  values of  $1.58 \pm 0.12$  (Salpeter IMF),  $1.05 \pm 0.08$  (Kroupa IMF, Kroupa 2001), and  $0.89 \pm 0.07$  (Chabrier IMF, Chabrier 2003). Fully consistent values are obtained if instead we use the age and metallicity found by Sánchez-Blázquez et al. (2006), i.e.,  $\log(\text{Age}) = 10.058 \pm 0.044$  and  $[Z/H] = 0.116 \pm 0.032$ .

We treat as a systematic error in §7.3 the additional (less well constrained) stellar mass contributions from non-central galaxies and intracluster light.

### 5.3. Dark Matter

We consider the following models for the distribution of DM. All the models possess two free parameters which may be expressed as a concentration  $c_\Delta$ , and mass  $M_\Delta$ , evaluated with respect to an overdensity  $\Delta$  times the critical density of the universe.

- **NFW** We adopt the NFW profile (Navarro et al. 1997) for our fiducial DM model since it is still the current standard both for modeling observations and simulated clusters.
- **Einasto** A more accurate model for  $\Lambda$ CDM halos is the Einasto profile (Einasto 1965). Our implementation for the Einasto profile follows Merritt et al. (2006), but we use Retana-Montenegro et al. (2012)’s approximation for  $d_n$ . We fix  $n = 5.9$  ( $\alpha = 0.17$ ) appropriate for a halo of mass similar to NGC 6482 (e.g., see figure 13 of Dutton & Macciò 2014).

- **CORELOG** Finally, we also investigate a pseudo-isothermal logarithmic potential with a core to provide a strong contrast to the NFW and Einasto models; i.e., a model having a constant density core but with a density that approaches  $r^{-2}$  at large radius. See §2.1.2 of Buote & Humphrey (2012c) for this model expressed in terms of  $c_\Delta$  and  $M_\Delta$ .

We evaluate all virial parameters (i.e.,  $c_\Delta$ ,  $M_\Delta$ , and  $r_\Delta$ ) at the redshift of NGC 6482. Note that the concentration values we quote below for the total mass profile (i.e., stars+gas+DM) employ the scale radius of the DM profile; i.e.,  $c_\Delta^{\text{tot}} \equiv r_\Delta^{\text{tot}}/r_s^{\text{DM}}$ , where  $r_s^{\text{DM}}$  is the DM scale radius and  $r_\Delta^{\text{tot}}$  is the virial radius of the total mass profile. To obtain  $r_\Delta^{\text{tot}}$  we begin with the DM interior to  $r_\Delta^{\text{DM}}$ , add in the baryonic components, and then recompute the virial radius. We iterate until the change in  $r_\Delta^{\text{tot}}$  is sufficiently small.

### 5.4. Adiabatic Contraction

We consider “adiabatic contraction” (AC) models that modify the shape of the DM halo due to the presence of the assembled stars in the central galaxy. The standard analytic AC model presented by Blumenthal et al. (1986) uses an adiabatic invariant,  $r_f M_f = r_i M_i$ , to connect the initial total mass profile (assumed to follow the unperturbed DM profile) and the final mass profile consisting of the central galaxy’s stellar mass and the perturbed DM profile. Blumenthal et al. (1986) assumed spherical symmetry and circular orbits. To allow for more complex AC models, we generalize the contraction factor  $r_f/r_i$  following Dutton et al. (2015),

$$\frac{r_f}{r_i} = a + b \left( \frac{M_i}{M_f} + c \right)^d, \quad (4)$$

where  $a$ ,  $b$ ,  $c$ , and  $d$  are constants. In Table 4 we list the parameters of the AC models we consider in this paper. In addition to the standard analytic model of Blumenthal et al. (1986, hereafter AC1), we investigate the analytic modification by Gnedin et al. (2004, hereafter AC2) that allows for non-circular orbits. Our implementation of AC2 uses the approximation suggested by Dutton et al. (2015). We denote by “AC3” the results of nominally standard cosmological hydrodynamical simulations by Dutton et al. (2015) that include cooling and star formation but not AGN feedback. Finally, we examine the “Forced Quenching” model (AC4) of Dutton et al. (2015) based on the same simulations as used for AC3 except that cooling and star formation are arbitrarily turned off at  $z = 2$ .

We implement the AC models by employing the iterative procedure described by Blumenthal et al. (1986) but using the generalized contraction factor in Equation (4). We neglect the hot gas for computing the contracted DM profile, which should be a good approximation since the gas mass is subdominant everywhere. In our present study we apply the AC models to the NFW and Einasto profiles. We quote results for the concentration parameters of these AC models using the scale radius of the initial unperturbed mass profile. Consequently, the quoted AC concentrations can be directly compared to the results of cosmological simulations with only DM (e.g., Dutton & Macciò 2014).

## 6. RESULTS

### 6.1. Overview

**Table 4**  
Adiabatic Contraction Model Definitions

Model	a	b	c	d	Description	Ref.
AC1	0	1	0	1	Standard	Blumenthal et al. (1986)
AC2	0	1	0	0.8	Modified	Gnedin et al. (2004)
AC3	1	-0.52	-1	2	Standard Hydro	Dutton et al. (2015)
AC4	0.75	0.25	0	2	Forced Quenching	Dutton et al. (2015)

**Note.** — Parameters refer to Equation 4. AC2 approximates Gnedin et al. (2004)’s modified AC model following Dutton et al. (2015). Both the Standard Hydro and Forced Quenching models refer to the results of cosmological hydrodynamical simulations at  $z = 0$ . The Forced Quenching model arbitrarily turns off cooling and star formation at  $z = 2$ . The AC models we compute in this paper use the NFW and Einasto profiles.

To fit the hydrostatic equilibrium model to the data we employ a Bayesian “nested sampling” analysis using the MultiNest code v2.18 (Feroz et al. 2009). We use a  $\chi^2$  likelihood function consisting of the surface brightness and temperature data in Table 3. We adopt flat priors on the free parameters except for  $P_{\text{ref}}$ , stellar mass ( $M_*$ ), and DM ( $M_{\text{DM}}$ ) for which we use flat priors on their logarithms. For each parameter we quote two “best” values: (1) the mean parameter value of the posterior, which we refer to as the “Best Fit”, (2) the parameter that maximizes the likelihood, which we refer to as the “Max Like”. Unless stated otherwise, errors quoted are the standard deviation ( $1\sigma$ ) of the posterior. Other than Figure 4, which evaluates the fiducial model using the Max Like parameters, all figures for the hydrostatic models plot the mean and standard deviation of the posterior as a function of radius for the quantity of interest; e.g., entropy, pressure, etc.

The fiducial model has 11 free parameters, which are as follows (see §5). Pressure boundary condition: 1 parameter ( $P_{\text{ref}}$ ). Entropy profile: 7 parameters ( $s_0, s_1, r_{b,1}, r_{b,2}, \alpha_1, \alpha_2, \alpha_3$ ). Stellar mass of the central galaxy: 1 parameter ( $M_*/L_K$ ). DM profile: 2 parameters ( $c_\Delta, M_\Delta$ ). We display the best-fitting fiducial model to the surface brightness and temperature profiles along with fractional residuals in Figure 4. The fit is generally excellent with almost all residuals within  $\approx 1\sigma$  of the model values. The most deviant data points are the last annuli for  $\Sigma_X$  for each data set (i.e., *Chandra* annulus 10 and *Suzaku* annulus 3), each of which lie  $\approx 1.6\sigma$  away from the best-fitting model. To provide a straightforward quantitative measure of goodness-of-fit we also perform a standard frequentist  $\chi^2$  analysis. We obtain  $\chi^2 = 9.7$  for 13 dof, which is formally acceptable. (For reference, if the stellar mass component of the central galaxy is omitted,  $\chi^2 = 20.0$ ; i.e., the data require it at  $3\sigma$  according to the F-test. If instead the DM profile is omitted,  $\chi^2 = 285.2$ , clearly demonstrating the failure of a mass-follows-BCG light model.)

Since we shall often refer to the “Best Fit” virial radii of the fiducial model, we list their values here:  $r_{2500} = 124 \pm 4$  kpc,  $r_{500} = 236 \pm 10$  kpc, and  $r_{200} = 340 \pm 15$  kpc. The extent of the data is  $\approx r_{2500}$  which we indicate in Figure 4.

### 6.2. Entropy

We show the entropy profile of the best-fitting fiducial hydrostatic model in Figure 5 and list the parameter measurements in Table 5. In the figure we plot the entropy scaled in terms of the quantity,  $S_{500} = 44.7$  keV cm<sup>2</sup> (see eqn. 3 of Pratt et al. 2010). The two breaks in the entropy profile occur at the locations of changes in slope of the temperature profile. The first break occurs near  $r = 9$  kpc where  $k_B T$  drops sharply, while the second break is near  $r = 50$  kpc where the

temperature profile inverts. Except for the region between the two break radii, where the entropy slope flattens somewhat, the slope of the entropy profile is consistent with that of the  $\sim r^{1.1}$  baseline model.

The entropy profile lies well above the baseline gravity-only model illustrating the role of energy injection from feedback processes. For comparison, we perform the scaling suggested by Pratt et al. (2010) where the entropy profile is multiplied by  $(f_{\text{gas}}/f_{b,U})^{2/3}$ , where  $f_{\text{gas}}$  is the cumulative gas fraction and  $f_{b,U} = 0.155$  is the cosmic baryon fraction. The result is shown in Figure 5 and indicates much better agreement between the rescaled entropy profile and the baseline profile interior to  $\approx r_{2500}$  and suggests that for  $r \lesssim r_{2500}$  the feedback energy injected into NGC 6482 has not raised the gas temperature but instead spatially redistributed the gas. These basic results are very consistent with those we have obtained previously for the massive isolated elliptical galaxies NGC 720 (Humphrey et al. 2011) and NGC 1521 (Humphrey et al. 2012b) and results for galaxy clusters (e.g., Pratt et al. 2010). In §8.4 we discuss the increasing deviation of the rescaled entropy profile from the baseline model exterior to  $r_{2500}$ .

Finally, for reference we note that the second break in the entropy profile is required statistically. Using a frequentist analysis, a one-break model yields a minimum  $\chi^2 = 24.2$  for 15 dof, so that the second break is required at a significance of  $\approx 3\sigma$  according to the F-test.

### 6.3. Pressure

We list the constraints on  $P_{\text{ref}}$  in Table 5 and plot the pressure profile for the fiducial hydrostatic model in Figure 5 scaled in terms of  $P_{500} = 1.80 \times 10^{-4}$  keV cm<sup>-3</sup> (see eqn. 5 of Arnaud et al. 2010) expressed as a total gas pressure (not electron pressure). For comparison we also display the “universal” pressure profile of Arnaud et al. (2010) determined from an analysis of galaxy clusters having  $M_{500} > 10^{14} M_\odot$ . The pressure profile of NGC 6482 is similar to (considering the intrinsic scatter) the universal profile of clusters for radii approximately  $0.1$ – $0.7 r_{500}$ , but exceeds it elsewhere. Despite significant differences, the broad agreement over a sizeable range in radius is noteworthy since the universal profile was calibrated for systems about 100 times more massive than NGC 6482. The increasing deviations of the observed profile from the universal one outside  $0.1$ – $0.7 r_{500}$ , however, demonstrate a significant breakdown of the mass scaling underlying the universal profile and points to the increasing importance of non-gravitational energy for group-scale halos.

### 6.4. Mass

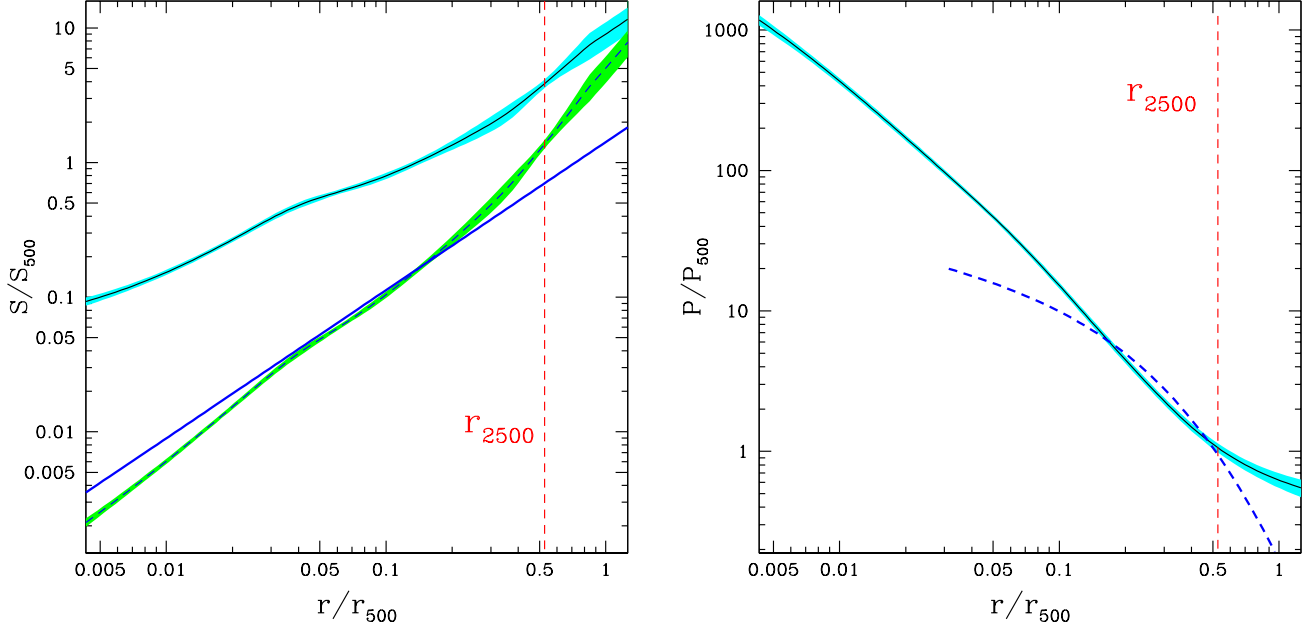


**Figure 5.** (Left Panel) Radial profile of the entropy (black) and  $1\sigma$  error region (cyan) for the fiducial hydrostatic model rescaled by  $S_{500} = 44.7 \text{ keV cm}^2$ . The baseline  $r^{1.1}$  profile obtained by cosmological simulations (Voit et al. 2005) with only gravity is shown as a blue line. The result of rescaling the entropy profile by  $\propto f_{\text{gas}}^{2/3}$  Pratt et al. (2010) is shown by the black dashed line (and green  $1\sigma$  region). (Right Panel) Radial profile of the gas pressure (black) and  $1\sigma$  error region (cyan) rescaled by  $P_{500} = 1.80 \times 10^{-4} \text{ keV cm}^{-3}$ . For comparison we also show the universal profile of Arnaud et al. (2010) derived for galaxy clusters.

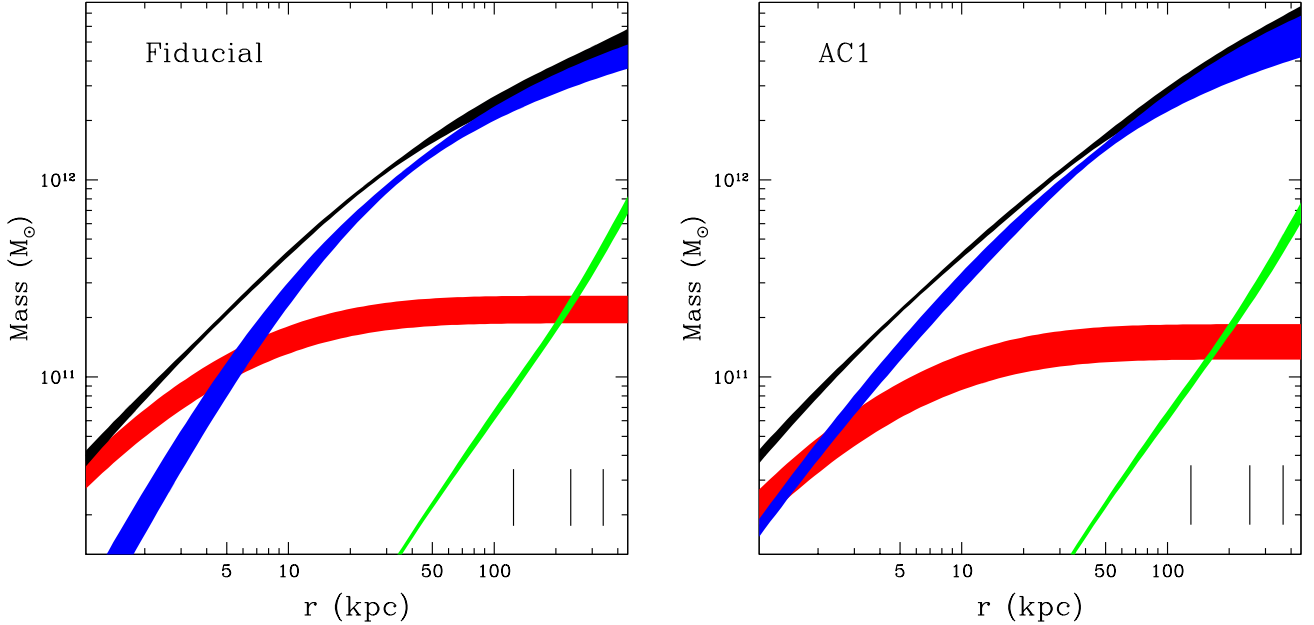


**Figure 6.** (Left Panel) Radial profiles of the total mass (black) and individual mass components of the fiducial hydrostatic model: total NFW DM (blue), stars (red), hot gas (green). The black vertical lines indicate the virial radii; i.e., from left to right:  $r_{2500}$ ,  $r_{500}$ , and  $r_{200}$ . (Right Panel) Same quantities plotted as in the Left Panel except for a hydrostatic model with an AC1 DM halo; i.e., an NFW DM halo modified by standard adiabatic contraction according to Blumenthal et al. (1986).

**Table 5**  
Pressure and Entropy

	$P_{\text{ref}}$ ( $10^{-1} \text{ keV cm}^{-3}$ )	$s_0$ ( $\text{keV cm}^2$ )	$s_1$ ( $\text{keV cm}^2$ )	$r_{b,1}$ (kpc)	$r_{b,2}$ (kpc)	$\alpha_1$	$\alpha_2$	$\alpha_3$
Best Fit (Max Like)	$2.18 \pm 0.19$ (2.29)	$2.33 \pm 0.70$ (1.77)	$1.76 \pm 0.55$ (2.08)	$8.81 \pm 1.87$ (10.24)	$52 \pm 27$ (23)	$1.11 \pm 0.16$ (1.02)	$0.55 \pm 0.17$ (0.34)	$1.38 \pm 0.41$ (1.02)

**Note.** — Best values and error estimates (see §6.1) for the free parameters of the pressure and entropy components of the fiducial hydrostatic equilibrium model.  $P_{\text{ref}}$  refers to the total gas pressure evaluated at the reference radius  $r = 1$  kpc and serves as the boundary condition for the hydrostatic model. The entropy parameters are defined in §5.1.

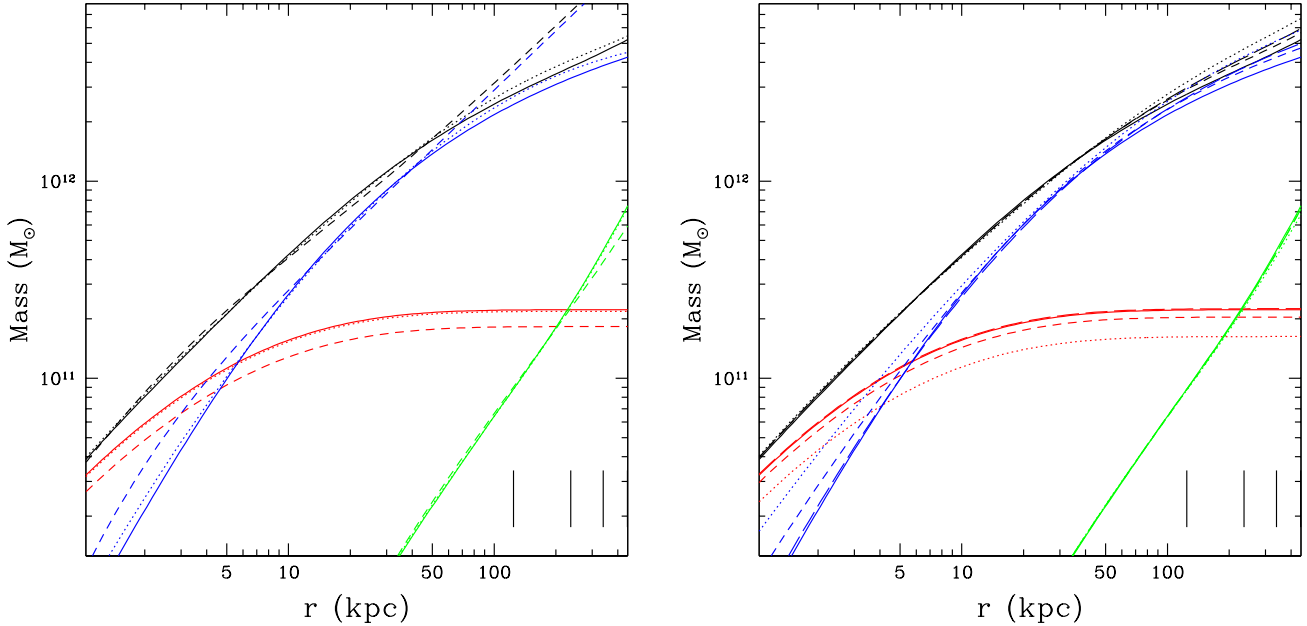


**Figure 7.** Radial mass profiles for hydrostatic models having different DM profiles: NFW (solid lines), Einasto (dotted lines), CORELOG (dashed lines). We show only the best-fitting models for clarity. The color scheme is the same as for Figure 6. The gas mass profiles are almost indistinguishable between the models. (*Right Panel*) Same quantities plotted as in the *Left Panel* except for hydrostatic models having adiabatically contracted DM halos: AC1 (dotted), AC3 (short dash), AC4 (long dash). AC2 (not shown) is very similar to AC1.

**Table 6**  
Stellar and Total Mass

	$M_*/L_K$ ( $M_\odot L_\odot^{-1}$ )	$c_{2500}$	$M_{2500}$ ( $10^{12} M_\odot$ )	$c_{500}$	$M_{500}$ ( $10^{12} M_\odot$ )	$c_{200}$	$M_{200}$ ( $10^{12} M_\odot$ )
Best Fit (Max Like)	$0.68 \pm 0.11$ (0.75)	$11.8 \pm 2.7$ (10.3)	$2.8 \pm 0.3$ (2.9)	$22.4 \pm 5.0$ (19.6)	$3.8 \pm 0.5$ (4.0)	$32.2 \pm 7.1$ (28.2)	$4.5 \pm 0.6$ (4.8)
Spherical	...	...	...	+0.4 -0.9	+0.07 -0.02	...	...
Einasto	-0.01	-1.2	0.3	-2.4	0.4	-3.7	0.4
CORELOG	-0.12	98.0	1.8	222.1	6.2	355.1	11.4
AC	-0.21	-3.9	0.4	-7.2	0.9	-10.3	1.2
BCG	+0.21 -0.15	+1.0 -1.8	+0.1 -0.0	+1.9 -3.3	+0.2 -0.1	+2.8 -4.8	+0.3 -0.1
Entropy	0.05	-1.4	0.1	-2.6	0.2	-3.7	0.3
Proj. Limit	0.03	-0.7	0.1	-1.4	0.1	-2.0	0.2
Distance	-0.06	-0.4	0.1	-0.7	0.2	-1.0	0.2
Frequentist	0.04	-1.0	0.1	-1.9	0.1	-2.6	0.2
$\Lambda_\nu(T, Z)$	0.04	2.0	-0.4	3.7	-0.6	5.6	-0.7
No Suzaku	-0.08	4.3	-0.5	8.0	-0.8	11.9	-0.9
Exclude Last Bin	0.03	-1.3	0.5	-2.5	0.8	-3.6	0.9
SWCX	0.01	0.1	-0.1	0.3	-0.1	0.5	-0.1
CXBSLOPE	+0.07 -0.02	+1.3 -2.0	+0.4 -0.3	+2.4 -3.7	+0.5 -0.4	+3.6 -5.4	+0.6 -0.4
NXB	-0.03	1.4	-0.2	2.6	-0.3	3.7	-0.4
$\chi^2$	-0.03	1.1	-0.2	2.0	-0.3	2.8	-0.3
$N_H$	0.02	-0.3	+0.0 -0.0	-0.5	+0.0 -0.0	-0.7	+0.1 -0.0
LMXBs	0.06	-1.8	0.1	-3.3	0.2	-4.7	0.3
Solar Abun.	+0.01 -0.01	+0.3 -0.3	+0.0 -0.1	+0.5 -0.6	+0.1 -0.1	+0.7 -0.9	+0.1 -0.1
Other Abun	0.06	-1.6	-0.0	-3.0	0.0	-4.3	0.0
1T Ann 1 Suzaku	-0.01	0.9	-0.2	1.6	-0.3	2.2	-0.4

**Note.** — Best values and error estimates (see §6.1) for the free parameters of the mass components of the fiducial hydrostatic equilibrium model; i.e., stellar mass-to-light ratio ( $M_*/L_K$ ), concentration, and enclosed total mass (stars+gas+DM). We show the concentration and mass results obtained within radii  $r_\Delta$  for overdensities  $\Delta = 200, 500, 2500$ . In addition, we give a detailed budget of systematic errors (§7). For each column we quote values with the same precision. In a few cases, an error has a value smaller than the quoted precision, and thus it is listed as a zero; e.g., “0.0” or “-0.0”. Briefly, the various systematic errors are as follows,

(“Spherical”, §7.1): spherical symmetry assumption  
 (“Einasto”, “CORELOG”, “AC” §7.4): Using different DM profiles: Einasto, CORELOG, or adiabatically contracted models  
 (“BCG”, §7.3): Allowing for a range of  $R_e$  for the BCG  
 (“Entropy”, §7.2): Variations of the entropy model  
 (“Proj. Limit”, §7.8): Varying the adopted outer radius for computing model projections  
 (“Distance”, §7.8): Using a different distance  
 (“Frequentist”, §7.8): Fit the hydrostatic equilibrium models using a standard  $\chi^2$  frequentist approach  
 (“ $\Lambda_\nu(T, Z)$ ”, §7.8): Using a parameterized model for the plasma emissivity  
 (“No Suzaku”, §7.8): Omitting the *Suzaku* data from the hydrostatic equilibrium model fits  
 (“Exclude Last Bin”, §7.8): Omitting the outer spectral bin from both the *Chandra* and *Suzaku* data in the hydrostatic equilibrium model fits  
 (“SWCX”, §7.5): Solar Wind Charge Exchange emission  
 (“CXBSLOPE”, §7.6): Varying the CXB power-law slope  
 (“NXB”, §7.6): Varying the normalization of the non-X-ray background model for the *Suzaku* data  
 (“ $\chi^2$ ”, §7.7): Minimizing  $\chi^2$  rather than the C-statistic for the spectral fitting  
 (“ $N_H$ ”, §7.7): Varying the Galactic hydrogen column density  
 (“LMXB”, §7.7): Varying the amount of emission from LMXBs in the spectral fitting  
 (“Solar Abun.”, §7.7): Using different solar abundance tables  
 (“Other Abun.”, §7.7): Allowing some abundance to vary with a non-solar ratio to iron  
 (“1T Ann 1 Suzaku”, §7.7): Using only a single temperature to model the spectrum of the central *Suzaku* annulus

We list in Table 6 the constraints on the mass parameters ( $M_*/L_K, c_\Delta, M_\Delta$ ) obtained for the fiducial hydrostatic model along with estimates for systematic errors (§7). We also plot the mass profiles for all sub-components in Figure 6. We quote the DM halo parameters evaluated for three overdensities,  $\Delta = 200, 500, 2500$ . Our hydrostatic models self-consistently evaluate the projection of gas for the entire system, and thus the data do constrain the gas for  $r \gtrsim r_{2500}$  albeit with less statistical precision and increased model dependence.

Considering only the statistical errors, the most weakly constrained mass parameter is the halo concentration (e.g.,  $\pm 22 - 23\%$ ), followed by the stellar mass ( $\pm 16\%$ ), and fi-

nally the total halo mass ( $\pm 11 - 13\%$ ). The gas mass profile is the most tightly constrained ( $\pm 6 - 12\%$ ). Most of the systematic errors induce parameter changes of the same size or smaller than the  $1\sigma$  statistical error and are therefore insignificant. The most significant changes in the parameters occur for the following systematic tests:  $M_*/L_K$  (BCG), concentration (No Suzaku), total mass (No Suzaku, Exclude Last Bin,  $\Lambda_\nu(T, Z)$ , CXBSLOPE). Since these largest effects lead to parameter changes of only  $\lesssim 1.5\sigma$ , we conclude that systematic errors, though important in some cases, do not dominate the error budget.

The stellar mass-to-light ratio of the BCG that we measure ( $M_*/L_K = 0.68 \pm 0.11$ , in solar units) agrees very well with

**Table 7**  
Results for Adiabatic Contraction Models

Model	$M_*/L_K$ ( $M_\odot L_\odot^{-1}$ )		$c_{200}$		$M_{200}$ ( $10^{12} M_\odot$ )		$f_{\text{gas},200}$		$f_{\text{b},200}$	
	Best	99%	Best	99%	Best	99%	Best	99%	Best	99%
Fiducial	0.68	(−0.28,+0.22)	32.2	(−13.9,+18.7)	4.5	(−1.1,+2.0)	0.099	(−0.030,+0.028)	0.149	(−0.038,+0.033)
AC1	0.49	(−0.17,+0.22)	19.6	(−12.8,+13.9)	6.1	(−2.1,+7.2)	0.082	(−0.043,+0.030)	0.110	(−0.053,+0.034)
AC2	0.51	(−0.21,+0.25)	22.6	(−15.2,+18.5)	5.7	(−1.9,+6.8)	0.086	(−0.044,+0.030)	0.117	(−0.055,+0.033)
AC3	0.62	(−0.20,+0.25)	28.4	(−15.9,+15.9)	5.0	(−1.3,+3.8)	0.093	(−0.037,+0.027)	0.134	(−0.048,+0.032)
AC4	0.68	(−0.25,+0.26)	23.0	(−12.9,+14.8)	5.3	(−1.5,+4.1)	0.091	(−0.038,+0.028)	0.135	(−0.050,+0.035)
Einasto	0.66	(−0.28,+0.26)	28.5	(−16.0,+18.4)	4.9	(−1.6,+4.3)	0.095	(−0.040,+0.031)	0.140	(−0.053,+0.038)
AC1	0.48	(−0.17,+0.20)	16.9	(−11.1,+14.3)	7.3	(−3.2,+8.2)	0.077	(−0.042,+0.034)	0.100	(−0.052,+0.040)
AC2	0.52	(−0.18,+0.22)	18.0	(−12.1,+14.2)	7.0	(−3.0,+8.4)	0.079	(−0.044,+0.033)	0.104	(−0.054,+0.039)
AC3	0.60	(−0.22,+0.27)	26.1	(−17.2,+17.8)	5.4	(−2.0,+6.8)	0.090	(−0.046,+0.031)	0.127	(−0.061,+0.038)
AC4	0.66	(−0.25,+0.27)	20.2	(−12.6,+14.7)	6.1	(−2.2,+6.4)	0.085	(−0.041,+0.032)	0.122	(−0.055,+0.039)

**Note.** — Best-fitting results and 99% confidence limits for selected mass parameters of the fiducial hydrostatic model, the model with an Einasto DM halo, and the corresponding AC models. The definitions of the AC models are given in Table 4.

our previous X-ray hydrostatic measurement (H06). However, this value of  $M_*/L_K$  lies below the estimates from the SPS models (§5.2) by  $1.9\sigma$  (Chabrier IMF),  $3.4\sigma$  (Kroupa IMF), and  $8.2\sigma$  (Salpeter) considering only the statistical error on the hydrostatic measurement. If the systematic error associated with the choice of the BCG effective radius is considered (i.e., BCG in Table 6), Then the best-fitting value rises to  $M_*/L_K = 0.89$  solar, which agrees very well with the SPS value for a Chabrier IMF and reasonably well for the Kroupa IMF. Hence, the hydrostatic analysis strongly favors SPS models with a Chabrier or Kroupa IMF over Salpeter, an issue to which we return in §8.3.

The halo concentration and mass were previously measured from hydrostatic X-ray studies by Khosroshahi et al. (2004) and H06. Khosroshahi et al. (2004) estimated  $M_{200} \approx 4 \times 10^{12} M_\odot$ , in good agreement with our result. But their estimate of  $c_{200} \sim 60$  far exceeds our value, as expected, because they neglected the mass of the BCG. In our previous analysis of H06 we did include the BCG but placed *ad hoc* restrictions on  $f_{\text{b},200}$ . For the case where the baryon fraction was restricted to the range  $0.032 \leq f_{\text{b},200} \leq 0.16$ , the fitted baryon fraction pegged at the upper limit ( $f_{\text{b},200} = 0.16^{+0.00}_{-0.10}$ ) so that  $c_{\text{vir}} = 38^{+76}_{-24}$  and  $M_{\text{vir}} = 3.6^{+5.5}_{-1.5} \times 10^{12} M_\odot$  computed within  $r_{103}$  (90% conf; see Table 4 of H06). If in our present study we use a similar radius (actually  $r_{102.3}$ ) we obtain  $c_{\text{vir}} = 42.2^{+16.7}_{-13.9}$  and  $M_{\text{vir}} = 5.2^{+1.4}_{-1.0} \times 10^{12} M_\odot$  (also 90% conf.) fully consistent with the very uncertain results of H06. However, unlike these previous measurements, which were extremely uncertain (no error bar quoted by Khosroshahi et al. 2004), here we have made a precise measurement revealing a high concentration that includes the BCG stellar mass and does not place *ad hoc* restrictions on the baryon fraction.

While our new measurement of  $c_{200} = 32.2 \pm 7.1$  is about half the value obtained by Khosroshahi et al. (2004) that neglected the stellar mass of the BCG, it is nevertheless very large when compared to simulated  $\Lambda$ CDM halos. For a “relaxed” DM halo with  $M_{200} = 4.5 \times 10^{12} M_\odot$  in the *Planck* cosmology Dutton & Macciò (2014) obtain  $c_{200} = 7.1$  with a log-normal intrinsic scatter of 0.11 dex. (In §8.1.1 we discuss the values obtained from other theoretical  $c_{200} - M_{200}$  relations.) Our measurement lies  $6\sigma$  above the mean  $\Lambda$ CDM relation in

terms of the intrinsic scatter and  $3.5\sigma$  above it in terms of the statistical error on the hydrostatic measurement. Such an extreme outlier would be difficult to reconcile with the  $\Lambda$ CDM simulations, and thus we examine whether modifications of the fiducial NFW DM halo can reduce significantly the inferred concentration. If instead we use the Einasto profile for the DM halo, we obtain  $c_{200} = 28.5 \pm 7.1$  and  $M_{200} = (4.9 \pm 1.1) \times 10^{12} M_\odot$ . For this mass and an Einasto profile, Dutton & Macciò (2014) obtain  $c_{200} = 8.1$  with an intrinsic scatter of 0.13 dex for  $\Lambda$ CDM halos. While somewhat less extreme of an outlier, our measurement using the Einasto profile still lies  $4.2\sigma$  above the mean  $\Lambda$ CDM relation in terms of the intrinsic scatter and  $2.9\sigma$  above it in terms of the statistical measurement error. Below we consider the AC models and especially their effect on the concentration and discuss the implications of the high concentration in §8.1.

We compare results for the fiducial (NFW), Einasto, and pseudo-isothermal CORELOG models in Figure 7. For all mass components over all radii plotted the NFW and Einasto models are extremely similar. The largest deviations between the two models occur only at the very smallest and largest radii plotted. The CORELOG model, however, displays substantial differences from the fiducial model. First, the stellar mass for CORELOG is lower (i.e., about  $1\sigma$ ) than NFW. Second, the DM exceeds the NFW profile both at small ( $\lesssim 10$  kpc) and large radii ( $\gtrsim 50$  kpc). Finally, the CORELOG total mass also exceeds the fiducial model for radii  $\gtrsim 50$  kpc. In good agreement with what we found previously for the fossil cluster RXJ 1159+5531 (Buote et al. 2016), the gas mass is very similar for all the models and the total mass “pinches” near  $1-2 R_e$  where the DM crosses over the stellar mass of the BCG so that the total mass is nearly identical for all the models there. Despite some large differences in the profiles of the different mass components, when we perform frequentist fits we obtain minimum  $\chi^2 = 9.7, 9.7, 9.4$  for 13 dof respectively for the NFW, Einasto, and CORELOG models; i.e., the X-ray data do not statistically distinguish the quality of the fits between the models.

Like the Einasto and CORELOG models, frequentist fits of the AC models with an NFW DM halo give minimum  $\chi^2$  values virtually the same as the fiducial model; i.e., the quality of the fits of the AC models is also statistically indistinguish-

**Table 8**  
Mass-Weighted Total Density Slope

Radius (kpc)	Radius ( $R_e$ )	$\langle\alpha\rangle$
1.8	0.5	$1.91 \pm 0.06$
3.6	1.0	$1.95 \pm 0.06$
7.3	2.0	$2.00 \pm 0.04$
18.2	5.0	$2.13 \pm 0.04$
36.5	10.0	$2.27 \pm 0.06$

**Note.** — These values refer to the application of Equation (5) to the fiducial hydrostatic model.

able from the fiducial model. In the right panel of Figure 6 we plot the mass profiles of the various components for AC1. The most notable features are the higher mass of DM within  $1-2 R_e$  and lower overall stellar mass compared to the fiducial model. These features are strongest for AC1 and AC2 compared to the other AC models. We compare the best-fitting mass profiles of the fiducial and AC models in Figure 7. Notice in particular that AC4 yields stellar mass and central DM mass profiles very similar to the fiducial model, but the DM and total mass of AC4 exceed those of the fiducial model at large radius.

In Table 7 we list the best-fitting results for  $M_*/L_K$ ,  $c_{200}$ , and  $M_{200}$  from the bayesian analysis along with their 99% confidence limits defined as the 0.5% and 99.5% values of the cumulative distributions obtained from the posterior. Generally, compared to the fiducial un-contracted model, the AC models give smaller  $M_*/L_K$ , smaller  $c_{200}$ , and larger  $M_{200}$ . The smaller concentrations are expected since they refer to the scale radius of the un-contracted NFW profile (§5.4); i.e., AC converts an initially lower concentration halo into a higher concentration halo, the latter of which is similar to what we measured above using the pure NFW profile. The AC1 and AC2 models give  $c_{200}$  values that are  $\approx 10$  less than the fiducial model but still  $> 4\sigma$  larger than expected for  $\Lambda$ CDM halos in terms of the intrinsic scatter. Moreover, their much smaller  $M_*/L_K$  values are difficult to reconcile with the SPS models for any IMF even considering reasonable systematic error associated with  $R_e$ . AC3 yields a more intermediate value for  $M_*/L_K$ , but its  $c_{200}$  is close to the fiducial value. AC4, however, gives  $M_*/L_K$  the same as the fiducial value while also yielding a smaller  $c_{200}$  that is a little less extreme of an outlier from the mean  $\Lambda$ CDM relation. As shown in Table 7, these results for the NFW DM halo (un-modified and AC) agree extremely well with those obtained for the Einasto DM halo (un-modified and AC). We discuss further the implications of the high concentration and AC models in §8.1.

### 6.5. Mass and Density Slopes

The total mass density profiles of massive elliptical galaxies are described accurately by  $\rho \sim r^{-\alpha}$  with  $\alpha \approx 2$  over a wide radial range; see, e.g., reviews of the evidence from X-ray hydrostatic equilibrium studies by Humphrey & Buote (2010) and from stellar dynamics and lensing by Courteau et al. (2014). It is now known this power-law relation extends to central BCGs in groups and clusters but with smaller  $\alpha$  (e.g., Humphrey & Buote 2010; Newman et al. 2013; Courteau et al. 2014; Cappellari et al. 2015, and references therein). The slope correlates with various structural properties including the stellar half-light radius of the

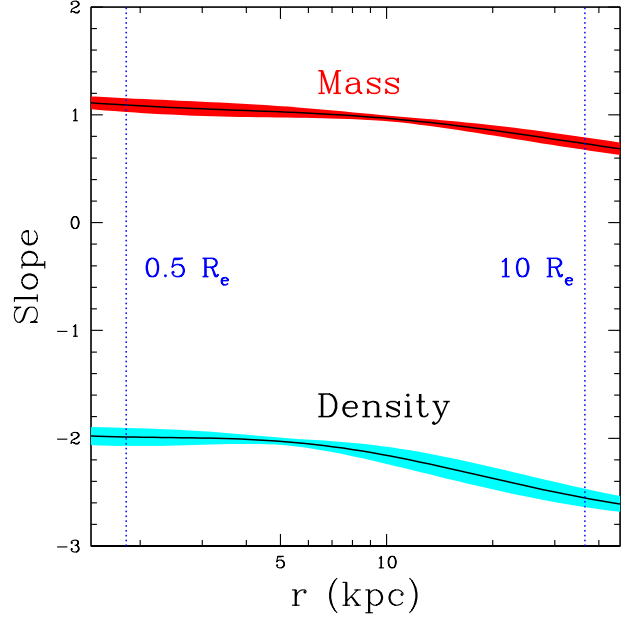


**Figure 8.** The radial profiles of the radial logarithmic derivatives (i.e., slopes) and  $1\sigma$  error regions of the total mass and total mass density for the fiducial hydrostatic model.

BCG. Using a toy model of a power-law total mass profile decomposed approximately into separate BCG stellar and NFW DM halos, Humphrey & Buote (2010) found that  $\alpha$  and  $R_e$  obey the following relation over radii  $0.2-10 R_e$ ,  $\alpha = 2.31 - 0.54 \log(R_e/\text{kpc})$ , in agreement with the relation obtained by Auger et al. (2010) for a larger galaxy sample analyzed with stellar dynamics and gravitational lensing.

We show in Figure 8 the slopes (i.e., radial logarithmic derivatives) of the radial profiles of the total mass and total mass density. Within  $\approx 2R_e$  the slopes of the mass and density are very slowly varying, and then they steepen more quickly at larger radii. Over radii  $0.5-10 R_e$  the slopes range from  $\approx 0.73 - 1.09$  for the mass to  $\approx -2.0$  to  $-2.55$  for the density, representing a radial density variation of almost 30%, with most of the variation occurring for radii  $\gtrsim 2R_e$ . Rather than fitting a power-law to the mass profile to obtain an average value for the slope, it is convenient to compute the mass-weighted total density slope  $\langle\alpha\rangle$  of our fiducial model following equation (2) of Dutton & Treu (2014),

$$\langle\alpha\rangle = 3 - \frac{d \ln M}{d \ln r}, \quad \alpha \equiv -\frac{d \ln \rho}{d \ln r}, \quad (5)$$

where  $M$  is the total mass enclosed within radius  $r$ . We list the mass-weighted slopes for selected radii between  $0.5-10 R_e$  in Table 8. The mass-weighted slope within  $10R_e$ ,  $\langle\alpha\rangle = 2.27 \pm 0.06$ , is  $\approx 12\%$  larger than the mean value  $\alpha = 2.02$  obtained using the  $\alpha-R_e$  scaling relation quoted above but is consistent within the observed scatter (Auger et al. 2010).

### 6.6. Gas and Baryon Fraction

In Figure 9 we show the radial profiles of the gas and baryon fractions for the fiducial hydrostatic model and quote the derived values and errors within  $r_{2500}$ ,  $r_{500}$ , and  $r_{200}$  in Table 9 along with the detailed systematic error budget. Similar to what we find for the mass profile (§6.4), most of the systematic errors for the gas and baryon fractions are insignif-



**Table 9**  
Gas and Baryon Fraction

	$f_{\text{gas},2500}$	$f_{\text{b},2500}$	$f_{\text{gas},500}$	$f_{\text{b},500}$	$f_{\text{gas},200}$	$f_{\text{b},200}$
Best Fit	$0.032 \pm 0.003$	$0.112 \pm 0.011$	$0.063 \pm 0.006$	$0.122 \pm 0.011$	$0.099 \pm 0.011$	$0.149 \pm 0.014$
(Max Like)	(0.030)	(0.115)	(0.062)	(0.124)	(0.099)	(0.151)
$M_{\text{other}}^{\text{stellar}}$	...	+0.046	...	+0.045	...	+0.043
Spherical	...	...	+0.0003 -0.0003	...	...	...
Einasto	-0.002	-0.010	-0.003	-0.009	-0.004	-0.008
CORELOG	-0.007	-0.046	-0.026	-0.066	-0.052	-0.090
AC	-0.003	-0.035	-0.008	-0.033	-0.014	-0.036
BCG	+0.000 -0.001 +0.000	+0.020 -0.018 0.001	+0.000 -0.002 +0.001	+0.013 -0.013 +0.001	+0.001 -0.003 -0.007	+0.009 -0.010 -0.006
Entropy	-0.001 +0.000 -0.001	0.001	+0.000 -0.001 0.002	+0.001 -0.001 -0.000	+0.001 -0.003 0.003	+0.001 -0.003 0.004
Proj. Limit	0.001	-0.001	0.001	0.002	0.003	0.004
Distance	-0.002	0.001	0.001	0.002	0.003	0.004
Frequentist	0.006	0.028	0.025	0.041	0.046	0.058
$\Lambda_{\nu}(T, Z)$	0.011	0.018	0.032	0.037	0.056	0.060
No Suzaku	-0.006	-0.011	-0.012	-0.017	-0.019	-0.023
Exclude Last Bin	0.002	0.005	0.007	0.009	0.014	0.015
SWCX	+0.005 -0.005	+0.011 -0.006	+0.014 -0.014 +0.004	+0.018 -0.016 0.006	+0.024 -0.025 +0.004	+0.027 -0.026 +0.007
CXBSLOPE	0.003	0.005	-0.002	0.006	-0.005	-0.003
NXB	0.002	0.004	0.001	0.003	-0.000	0.002
$\chi^2$	0.001	0.002	0.000	0.001	+0.000 -0.000	+0.001 -0.001
$N_{\text{H}}$	+0.000 -0.002	+0.006 -0.003	-0.006	+0.002 -0.007	-0.011	+0.001 -0.012
LMXBs	-0.003	+0.000 -0.001	-0.005	-0.004	-0.007	-0.006
Solar Abun.	-0.005	0.004	-0.009	-0.003	-0.013	-0.008
Other Abun	0.004	0.009	0.005	0.009	0.006	0.009
1T Ann 1 Suzaku						

**Note.** — Best values and error estimates (see §6.1) for the gas and baryon fractions of the fiducial hydrostatic equilibrium model quoted for several overdensities.  $M_{\text{other}}^{\text{stellar}}$  refers to the addition of non-central stellar baryons (§7.3). See the notes to Table 6 regarding the other systematic error tests.

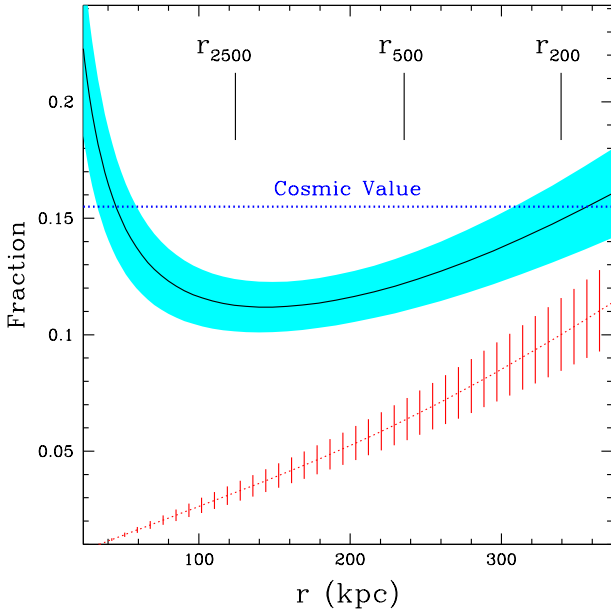


**Figure 9.** Baryon fraction (solid black line, shaded cyan  $1\sigma$  error region) and gas fraction (dotted red line, shaded red  $1\sigma$  error region) of the fiducial hydrostatic model.

icant, and the most important effects occur for the systematic tests, No Suzaku, Exclude Last Bin,  $\Lambda_{\nu}(T, Z)$ , CXBS-

LOPE. These largest effects testify to the sensitivity of the gas and baryon fractions to the accuracy of the surface brightness and temperature at the largest radii in our study (i.e., near  $r_{2500}$ ) determined primarily by the *Suzaku* measurements of the background-dominated group X-ray emission. (See §7 and §8.2.)

For  $r_{2500}$  and  $r_{500}$  the baryon fraction of the fiducial hydrostatic model yields,  $f_{\text{b}} < f_{\text{b},\text{U}}$ , where  $f_{\text{b},\text{U}} = 0.155$  is the mean baryon fraction of the universe as determined by *Planck* (Planck Collaboration et al. 2014). At  $r_{200}$ , we obtain  $f_{\text{b},200} = 0.149 \pm 0.014$ , consistent with  $f_{\text{b},\text{U}}$ , and where the hot gas comprises 67% of the total baryons. The Einasto model yields results very similar to the fiducial NFW model, whereas CORELOG has a much smaller value,  $f_{\text{b},200} = 0.06 \pm 0.01$ , owing to its larger total mass. Similarly, since the AC models also yield larger total masses than the fiducial model, they also produce smaller gas and baryon fractions (Table 7), where the largest effect is for AC1; e.g.,  $f_{\text{b},200} = 0.110 \pm 0.017$ .

Thus far we have only considered the stellar baryons of the BCG as indicated by the fitted  $M_{\star}/L_K$ . In §7.3 we estimate the amount of non-central stellar baryons and list the results ( $M_{\text{other}}^{\text{stellar}}$ ) as a systematic error in Table 9. The addition of these non-central stellar baryons increases the baryon fraction to  $\approx f_{\text{b},\text{U}}$  for  $r_{2500}$  and  $r_{500}$ . However, at  $r_{200}$  the value becomes  $f_{\text{b}} \approx 0.19$  which exceeds the cosmic value with  $\approx 2.5\sigma$  statistical significance. Although the excess is marginally significant (and other systematic effects do mitigate the difference further), if our estimates for the contributions from the non-central baryons are accurate, then the super-cosmic baryon fraction at  $r_{200}$  for the fiducial model provides evidence in

support of the AC models and their smaller baryon fractions.

### 6.7. MOND

For comparison to our standard Newtonian analysis with a DM halo, we also consider the most widely investigated and successful modified gravity theory, MOND (Milgrom 1983). Despite its many successes, MOND is presently unable to explain the mass profiles of galaxy clusters without DM (e.g., Sanders 1999; Pointecouteau & Silk 2005; Angus et al. 2008; Milgrom 2015). To determine whether this also applies to NGC 6482, we use the approach of Angus et al. (2008) that is based on Sanders (1999).

Following Sanders (1999), we assume spherical symmetry and associate the gravitational acceleration derived from the equation of hydrostatic equilibrium,

$$\vec{g}_{\text{HE}} = \frac{\hat{r}}{\rho} \frac{dP}{dr}, \quad (6)$$

with the general acceleration independent of the gravity theory. (Note – in Buote et al. 2016 we referred to the magnitude of this quantity as  $g_{\text{N}}$ .) For a spherical system, the MONDian gravitational acceleration ( $\vec{g}_{\text{M}}$ ) is related to the enclosed MONDian mass ( $M_{\text{M}}(< r)$ ) by the relation (Milgrom 1983; Bekenstein & Milgrom 1984),

$$-GM_{\text{M}} \frac{\hat{r}}{r^2} = \mu(g_{\text{M}}/a_0) \vec{g}_{\text{M}}, \quad (7)$$

where  $g_{\text{M}} \equiv |\vec{g}_{\text{M}}|$ ,  $a_0 \approx 1.2 \times 10^{-8} \text{ cm s}^{-2}$  is the MOND acceleration constant, and  $\mu(g_{\text{M}}/a_0)$  is some unspecified function interpolating between the Newtonian and MONDian regimes. Replacing  $\vec{g}_{\text{M}}$  with  $\vec{g}_{\text{HE}}$  in Equation (7), and using the simple interpolating function,  $\mu(x) = x/(1+x)$ , we have,

$$\frac{GM_{\text{M}}}{r^2} = \frac{g_{\text{HE}}}{1 + a_0/g_{\text{HE}}}, \quad (8)$$

where  $g_{\text{HE}} \equiv |\vec{g}_{\text{HE}}|$  and we have made use of the relation,  $\vec{g}_{\text{M}} = -g_{\text{M}} \hat{r}$ .

Since we have already computed  $g_{\text{HE}}(r)$  in our Newtonian analysis, we may immediately compute  $M_{\text{M}}(< r)$  without any additional fitting. The use of the simple interpolating function  $\mu$  in Equation (8) means our solutions have the undesirable feature that  $M_{\text{M}}(< r)$  attains a maximum value at some radius and then decreases (for additional discussion of this issue see Angus et al. 2008). Presently, we discuss results interior to the radius roughly where the MONDian mass profile attains its maximum.

We plot the cumulative DM fractions ( $M_{\text{DM}}/M_{\text{total}}$ ) in Figure 10 for the fiducial hydrostatic model computed in the context of both Newtonian and MONDian gravity. The Newtonian DM fraction rises continuously with radius whereas the MONDian DM fraction attains its maximum value for  $r \approx 35 \text{ kpc}$ . At this radius the DM dominates the MONDian mass profile with a DM fraction  $0.68 \pm 0.05$ . Using an estimate for the contribution from non-central baryons (§7.3) reduces the MOND DM fraction to  $\approx 0.59$ . The MOND DM fraction is reduced an additional 0.09 if we use the upper limit for  $R_e$  for the BCG (§5.2); i.e., MOND still needs as much DM as baryonic matter.

It is instructive to examine what a Newtonian analysis should have yielded for the mass profile in a MOND gravity

field without DM. Solving Equation (8) for  $g_{\text{HE}}$  gives,

$$g_{\text{HE}} = \frac{GM_{\text{M}}}{2r^2} \left( 1 + \sqrt{1 + 4 \frac{a_0 r^2}{GM_{\text{M}}}} \right). \quad (9)$$

(Note – in Buote et al. 2016 we referred to  $GM_{\text{M}}(< r)/r^2$  in this equation as  $g_{\text{M}}$ .) If we take  $M_{\text{M}}$  to be the sum of the enclosed masses of the baryonic components (i.e., stellar and gas) and identify  $g_{\text{HE}}$  with  $GM_{\text{N}}(< r)/r^2$  as appropriate for a Newtonian analysis, then we may use Equation (9) to predict the Newtonian mass profile that one would infer for a MONDian gravity field generated only by the baryonic mass components. For this exercise, we take the stellar and gas mass profiles obtained from our fiducial model (i.e., Newtonian analysis), combine them to give  $M_{\text{M}}(< r)$ , and then use Equation (9) to compute  $M_{\text{N}}(< r)$  that MOND would predict. In Figure 10 we compare this predicted Newtonian total mass profile to the one actually measured. The profile predicted by MOND without DM underestimates the true Newtonian profile out to  $\approx r_{2500}$  at which point it crosses over, and then exceeds, the Newtonian profile for larger radii. The largest underestimate occurs again near a radius  $\approx 35 \text{ kpc}$  where  $M_{\text{M}} \approx 0.48 M_{\text{N}}$ . Accounting for the non-central baryons and using the upper limit for  $R_e$  for the BCG increases this value to  $M_{\text{M}} \approx 0.65 M_{\text{N}}$ .

We conclude that MOND requires substantial amounts of DM to explain the X-ray emission of NGC 6482, consistent with results obtained for more massive groups and clusters.

### 6.8. Super-Massive Black Hole

We note the good fit to the centrally peaked temperature profile<sup>4</sup> by the fiducial model that does not include the mass of any putative super-massive black hole (SMBH). That is, the stellar mass density is sufficiently centrally peaked to produce the temperature peak in NGC 6482, as was shown previously by Humphrey et al. (2006) for this system and two other elliptical galaxies (NGC 720 and NGC 4125) with centrally peaked temperature profiles. For the early-type galaxy NGC 1332, which also has a centrally peaked temperature profile, Humphrey et al. (2009a) showed that adding an SMBH with a plausible mass did little to alter the central temperature over that established by the stellar potential. Only for the massive elliptical galaxy NGC 4649, for which the sphere of influence is largely resolved by *Chandra*, is there a strong case for a central X-ray temperature peak generated by the potential of the SMBH (Humphrey et al. 2008; Brighenti et al. 2009; Paggi et al. 2014).

From analysis of a large cosmological simulation, Raouf et al. (2016) find evidence that the BCGs in fossil systems should possess SMBHs with above-average masses. Visual inspection of Figure 6 of Raouf et al. (2016) indicates that NGC 6482 would possess an SMBH with  $M_{\text{bh}} \sim 10^9 M_{\odot}$ . Using this  $M_{\text{bh}}$  along with the central stellar velocity dispersion of the BCG ( $\sigma = 310.4 \pm 11.5 \text{ km s}^{-1}$ ; Ho et al. 2009), the sphere, or radius, of influence of the SMBH is  $r_g = GM_{\text{bh}}/\sigma^2 \sim 0.05 \text{ kpc}$ ; i.e.,  $r_g$  is only  $\sim 4\%$  of the radius of *Chandra* Annulus 1 (Table 3). Consequently, when we add an SMBH with  $M_{\text{bh}} = 10^9 M_{\odot}$  to our hydrostatic models there

<sup>4</sup> We also mention that centrally peaked temperature profiles in massive elliptical galaxies can be explained by classical wind models (e.g., David et al. 1991; Ciotti et al. 1991) without needing to invoke additional energy input from an AGN.

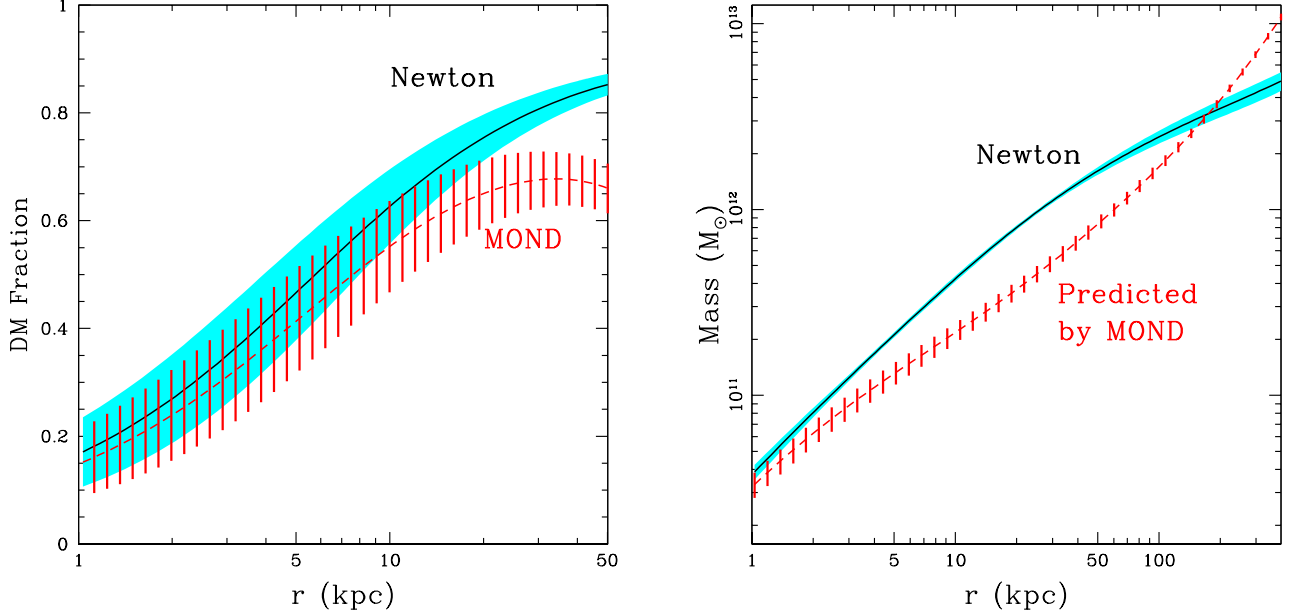


**Figure 10.** (Left Panel) Radial profiles of the DM fraction for the fiducial hydrostatic model for the Newtonian (black and cyan) and MOND (red) cases. The shaded and hashed regions represent  $1\sigma$  errors. (Right Panel) Total Newtonian mass profiles of (1) the fiducial hydrostatic model (black and cyan, same as in Fig.6), and (2) that predicted by MOND without DM (red) from eqn. 9.

is no tangible effect. We find that our model fits are only affected noticeably when  $r_g$  is at least about half the radius of Annulus 1 corresponding to  $M_{bh} > 10^{10} M_\odot$ , though even then the statistical significance is weak. Hence, presently we are unable to place interesting constraints on  $M_{bh}$ .

## 7. ERROR BUDGET

Here we describe various systematic errors and their impact on our analysis. The detailed error budget is listed for the mass parameters in Table 6 and gas and baryon fractions in Table 9.

### 7.1. Spherical Symmetry

To estimate the magnitude of possible systematic error due to the assumption of spherical symmetry, we use the results of Buote & Humphrey (2012c) who examined the orientation-averaged biases (mean values and scatter) of several quantities derived from spherically averaged hydrostatic equilibrium studies of hot gas in ellipsoidal galaxy clusters. We use the “NFW-EMD” results for the halo concentration, total mass, and gas fraction from Table 1 of Buote & Humphrey (2012c) to estimate the average error arising from assuming spherical symmetry within a radius of  $r_{500}$  when the system is really an ellipsoid viewed at a random orientation. We adopt an intrinsic flattening of  $q \approx 0.6$  based on cosmological simulations of DM halos with mass similar to NGC 6482 (Schneider et al. 2012). In all cases the derived systematic errors (“Spherical”) on the concentration, mass, and gas fraction within  $r_{500}$  listed in Tables 6 and 9 are insignificant.

### 7.2. Entropy Model

We considered the systematic effects (“Entropy”) of two modifications to the default entropy profile having two break radii. For one test we set  $r_{baseline} = 400$  kpc; i.e., twice the default value. For the other test we added a third break radius to the entropy profile. In each case the induced systematic error is everywhere insignificant.

### 7.3. Stellar Mass

We studied the full range of estimated uncertainty in  $R_e$  for the BCG stellar mass model (Table 1; §5.2) and its impact on the derived hydrostatic equilibrium models (“BCG”). We discussed the magnitudes of the systematic errors in §6.4 and §6.6. The most important effect is on  $M_*/L_K$  by allowing larger values that bring the measured values into better agreement with SPS models (§6.4).

The amounts and distributions of non-central stellar baryons (i.e., non-central galaxies and diffuse intracluster light (ICL)) are more uncertain than for the BCG, and therefore we prefer to treat their contributions to the total baryon fraction as a systematic error similar to our previous study of the fossil cluster RXJ 1159+5531 (Buote et al. 2016). Lieder et al. (2013) present a catalog of 48 group members of NGC 6482 from deep  $B$ - and  $R$ -band imaging. Using their measured  $M_R$  for each galaxy, we find that the non-central galaxies constitute 28% of the  $R$ -band stellar light of the group. For our calculation we assume this result also applies in the  $K$  band with the same  $M_*/L_K$  as the BCG. Since we lack an ICL measurement for NGC 6482, we use the result of Budzynski et al. (2014) that typically the ICL in groups and clusters is  $\approx 30\%$  of the total stellar mass fraction. We assume that the non-central galaxies and ICL follow the spatial distribution of the DM in our models.

We list the contribution of the non-central baryons to the baryon fraction as “ $M_{stellar}^{other}$ ” in Table 9. This is one of the largest systematic effects (§6.6) and lends support to the AC models which have smaller baryon fractions.

### 7.4. DM Model

The effects of using a DM profile different from NFW are indicated in the rows “Einasto”, “Corelog”, and “AC” in Tables 6 and 9. The “AC” column includes the results of all 4 AC models (Table 4) applied to the NFW DM profile, though the results are dominated by AC1. We have discussed the magnitudes of these systematic differences in §6.4 and §6.6.

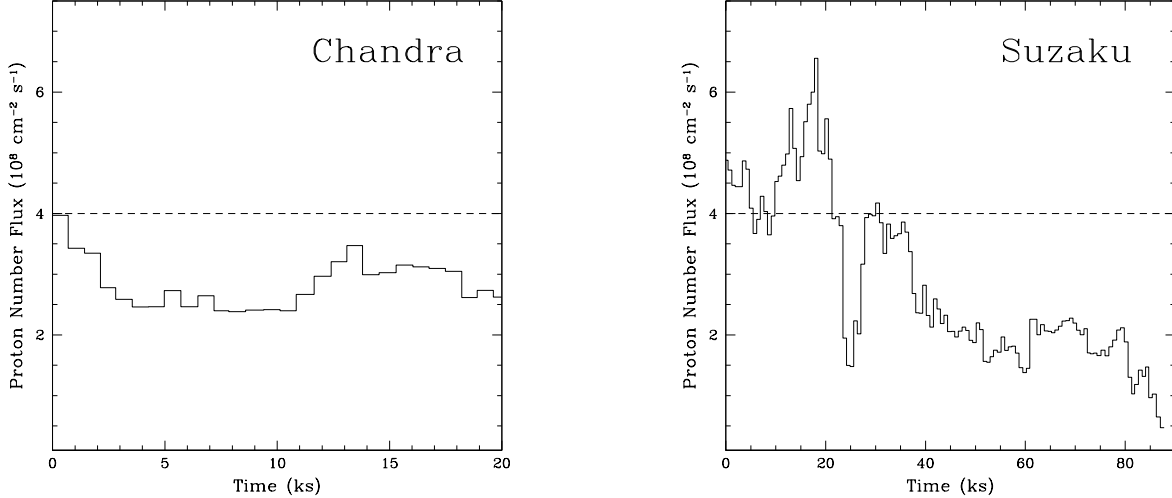


**Figure 11.** Solar proton flux measured by SWEPAM/SWICS during the (Left Panel) *Chandra* and (Right Panel) *Suzaku* observations of NGC 6482. The dashed line denotes the approximate level suggested by Fujimoto et al. (2007) above which SWCX emission may significantly contaminate *Suzaku* data.

### 7.5. SWCX

To investigate whether the *Chandra* and *Suzaku* observations may have been impacted by enhanced SWCX emission we examined the solar proton flux using the Level 3 data from SWEPAM/SWICS<sup>5</sup>. In Figure 11 we plot the solar proton flux observed by SWEPAM/SWICS during the *Chandra* and *Suzaku* observations for NGC 6482, which includes the periods of time gaps over the duration of the *Suzaku* observation, and we have accounted for the travel time from the satellite to Earth. Almost all the *Chandra* observation has solar proton flux below  $4 \times 10^8 \text{ cm}^{-2} \text{ s}^{-1}$ , which is approximately the level suggested by Fujimoto et al. (2007) above which significant proton flare contamination of *Suzaku* observations can be expected. However, the initial  $\sim 25\%$  of the *Suzaku* observation does exceed this flux level indicating possibly important SWCX flare contamination.

As noted in §2.1 and §2.2, the light curves for both the *Chandra* and *Suzaku* observations are very quiescent and provide no evidence of significant flaring. In addition, following our previous study of the fossil cluster RXJ 1159+5531 (Su et al. 2015) we investigated including a spectral model for the SWCX emission in each of the *Chandra* and *Suzaku* data and found no evidence for significant SWCX emission. Finally, when removing all the time intervals with solar proton flux above  $4 \times 10^8 \text{ cm}^{-2} \text{ s}^{-1}$  in the *Suzaku* data, the total cleaned exposure time is reduced substantially; i.e., by 25% to 32.6 ks. For these reasons, and remembering that the key  $4 \times 10^8 \text{ cm}^{-2} \text{ s}^{-1}$  flux level does not guarantee strong flare contamination, we do not use the nominally SWCX-cleaned data set for *Suzaku* by default. Instead, we treat it as a systematic error (“SWCX”) in Tables 6 and 9. For the mass parameters (i.e.,  $M_*/L_K$ , concentration, and mass) the effect is insignificant in all cases. For the gas and baryon fractions, the effect is comparable to the  $1\sigma$  errors leading to slightly larger values.

### 7.6. Background

In addition to SWCX, we examined other systematic effects associated with the characterization of the background.

First, we varied the *Suzaku* NXB model emission by  $\pm 5\%$  to gauge how sensitive are the results to the default level. We find that all induced changes are statistically insignificant – see row “NXB” in Tables 6 and 9. Second, for both the *Chandra* and *Suzaku* data we examined the sensitivity of the results to the value of the CXB power-law slope (i.e.,  $\Gamma = 1.41$ ). When changing the slope to  $\Gamma = 1.3$  and  $\Gamma = 1.5$ , representing approximately the range of observed values (e.g., Tozzi et al. 2001; De Luca & Molendi 2004; Moretti et al. 2009), we obtain the results listed in row “CXBSLOPE” in the tables. As noted above in §6.4 and §6.6, this is among the largest systematic errors. In most cases the differences are  $\sim 1\sigma$  or a little less. The largest differences are  $\sim 2\sigma$  and occur for the gas and baryon fractions at  $r_{200}$ .

### 7.7. Miscellaneous Spectral Fitting

Here we summarize other tests involving the spectral analysis. We varied the adopted value of Galactic  $N_H$  by  $\pm 20\%$  (“ $N_H$ ”) finding the effect to be insignificant. Likewise, minimizing  $\chi^2$  instead of the C-statistic (“ $\chi^2$ ”) did not affect the parameters significantly. By default we use two temperatures to model the gas emission within the central *Suzaku* annulus (§3.3). If instead we use a single temperature, we obtain the results listed in row “1T Ann1 *Suzaku*” in Tables 6 and 9. The induced changes are generally insignificant for  $M_*/L_K$ , the concentrations, and total masses, but are possibly significant ( $\lesssim 1\sigma$ ) for the gas and baryon fractions.

We also examined how choices regarding the metal abundances affect the results. First, we examined using different solar abundance tables (Grevesse & Sauval 1998; Lodders 2003) than our default (Asplund et al. 2006) and list the results in the “Solar Abun” row in Tables 6 and 9. The induced changes are insignificant. The results of using spectral fits allowing Ne, Mg, and Si to vary with non-solar ratios with respect to Fe are listed in the row “Other Abun.” This effect is insignificant in most cases, except for the gas fractions where  $\approx 1\sigma$  smaller gas fractions are indicated.

Finally, we considered various permutations of our treatment of the LMXB component in the spectral fits. That is, for each observation we performed fits both with the flux of the LMXB component set to a nominal value and with it freely fitted (§3.1.1). We chose by default to use the nominal LMXB

<sup>5</sup> [http://www.srl.caltech.edu/ACE/ASC/level2/sweswi\\_l3desc.html](http://www.srl.caltech.edu/ACE/ASC/level2/sweswi_l3desc.html)

flux for the *Chandra* spectral fits and the freely fitted LMXB flux for the *Suzaku* fits. As a systematic test, we used various permutations of these choices (i.e., nominal LMXB flux for both, freely fitted for both) and list the results in the row “LMXB” in the tables. The effect is only weakly significant for the gas and baryon fractions leading to  $\approx 1\sigma$  smaller values

### 7.8. Miscellaneous Hydrostatic Modeling

In this section we describe additional tests regarding details of the hydrostatic equilibrium models. First, we examined the sensitivity of our models to the assumed distance to NGC 6482 by instead using the distance employed by Ma et al. (2014) but scaled to  $H_0 = 70 \text{ km s}^{-1} \text{ Mpc}^{-1}$  (i.e., 62.3 Mpc). We list the results in Tables 6 and 9 in row “Distance” and find the effect to be insignificant in all cases. Second, we examined the sensitivity of our results to the assumed maximum radius (1 Mpc) used to define the hydrostatic equilibrium model. In row “Proj. Limit” of Tables 6 and 9 we show the results of using 0.75 Mpc or 1.5 Mpc for the maximum radius and find that in all instances the effect is insignificant. Next we explored the result of performing a standard  $\chi^2$  frequentist analysis for the hydrostatic equilibrium models (i.e., as opposed to the default nested sampling bayesian approach) and list the results in row “Frequentist” in the tables. Again, in all cases the effect is insignificant.

We also considered how the results changed by excluding some of the data. The results obtained from excluding the outer annulus from each of the *Chandra* and *Suzaku* data sets (i.e., annulus 10 and annulus 3 respectively) are listed in row “Exclude Last Bin” in Tables 6 and 9. This is one of the largest systematic effects investigated leading to differences of  $\sim 1.5\sigma$  significance in  $M_{200}$  and  $f_{b,200}$ . Unsurprisingly, the largest effects occur for the largest radius considered (i.e.,  $r_{200}$ ). Even larger differences are observed when the *Suzaku* data, which extend out the largest radius in our study, are omitted entirely (“No *Suzaku*”). As expected, the differences manifested when omitting the *Suzaku* data increase with increasing radius; e.g.,  $c_{200}$  increases and  $M_{200}$  decreases at  $\sim 1.5\sigma$  significance. The baryon fraction changes even more, such that  $f_{b,200}$  increases by  $\sim 4\sigma$  (with respect to the error bar of the fiducial model) to a super-cosmic value of  $\sim 0.21$ . Note, however, that omitting the *Suzaku* data increases the error bar so that  $f_{b,200}$  formerly exceeds the cosmic value at a lower significance level ( $\sim 2.5\sigma$ ).

Finally, we considered the effect of fitting the radial iron abundances (Table 3) with a projected, emission-weighted parameterized model that is used in the evaluation of the plasma emissivity  $\Lambda_\nu(T, Z)$  (§4). For the parameterized model we used a multi-component model related to that consisting of two power-laws mediated by an exponential (eqn. 5 of Gastaldello et al. 2007) and a constant floor. We list the results for this test of the plasma emissivity in row “ $\Lambda_\nu(T, Z)$ ” of Tables 6 and 9. This is one of the largest systematic effects and induces parameter shifts very similar to the “No *Suzaku*” test. Apparently, the parameterized model fit for the iron abundance is dominated by the *Chandra* measurements at the largest radii because of the large *Suzaku* error bar on the iron abundance (Table 3). The smaller *Chandra* abundances lead to smaller plasma emissivity and higher gas density at large radius. The higher gas density translates to higher gas and baryon fractions. Indeed, if we use the fitted model for the iron abundance, but omit the *Suzaku* data entirely, then

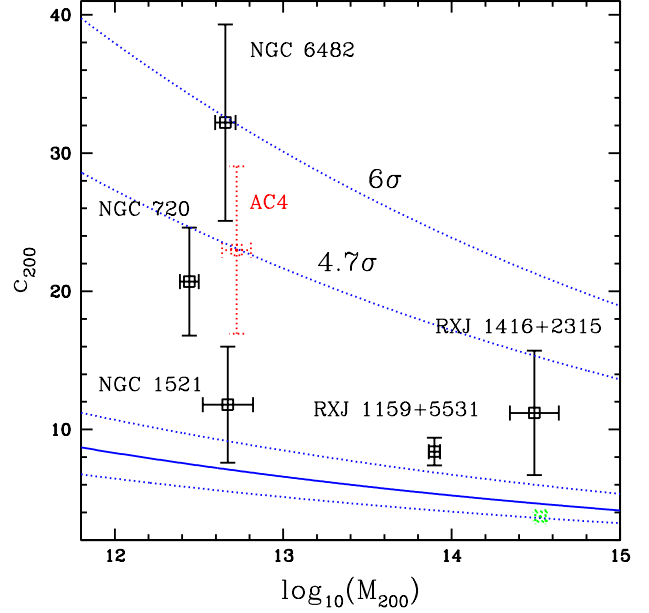


**Figure 12.** Concentration and mass values for NGC 6482 and other fossil systems (see §8.1). The blue solid line is the  $\Lambda$ CDM relation for relaxed halos from Dutton & Macciò (2014) evaluated at the distance of NGC 6482. The blue dotted lines indicate the intrinsic scatter in the  $\Lambda$ CDM relation; i.e., the lines closest the mean relation are  $\pm 1\sigma$  while the significances of the other lines are indicated. The data point indicated by red dots is obtained for the “Forced Quenching” AC NFW model (i.e., AC4 – Tables 4 and 7). Finally, the green dotted data point is our preliminary measurement for RXJ 1416+2315 using more recent data.

the parameter differences with respect to the fiducial model are all insignificant. Thus, the “No *Suzaku*” and “ $\Lambda_\nu(T, Z)$ ” tests demonstrate the importance of obtaining more accurate iron abundance measurements at large radius ( $\gtrsim r_{2500}$ ) to obtain robust measurements of the mass parameters, especially the gas and baryon fractions (§8.2).

## 8. DISCUSSION

### 8.1. High Concentration and Adiabatic Contraction

In §6.4 we found that the halo concentration for the fiducial model with an NFW DM profile ( $c_{200} = 32.2 \pm 7.1$ ,  $M_{200} = (4.5 \pm 0.6) \times 10^{12} M_\odot$ ), though only about half the original estimate of  $c_{200} \sim 60$  obtained by Khosroshahi et al. (2004) who did not include a separate BCG stellar component, nevertheless significantly exceeds the value of  $c_{200} = 7.1$  expected for relaxed  $\Lambda$ CDM halos (Dutton & Macciò 2014); i.e., by  $6\sigma$  with respect to the intrinsic scatter in the theoretical  $\Lambda$ CDM  $c-M$  relation and by  $3.5\sigma$  with respect to the statistical measurement error for the observations. Moreover, from visual inspection of Figure 16 of Dutton & Macciò (2014), which shows  $c_{200}$  and  $M_{200}$  obtained from NFW fits to simulated  $\Lambda$ CDM halos, we notice that for the mass of NGC 6482 there are no  $\Lambda$ CDM halos with  $c_{200} > 30$ . While the observational error on  $c_{200}$  permits smaller values, the measured  $c_{200}$  and  $M_{200}$  values for the fiducial model with an NFW DM halo represent an extremely rare system formed in  $\Lambda$ CDM. (Note, however, that otherwise the DM profile does not appear to be unusual; e.g., (1) we measure a DM fraction within  $5R_e$  of  $74\% \pm 5\%$  for NGC 6482 that is very consistent with other massive elliptical galaxies (e.g., Alabi et al. 2016); (2) the slope of the total mass profile is consistent with the  $\alpha-R_e$  scal-

ing relation within the observed scatter (§6.5.)

We plot in Figure 12 the  $c_{200}$  and  $M_{200}$  values for NGC 6482 and a few other fossil and nearly fossil systems with evidence for above-average concentrations: NGC 720 (Humphrey et al. 2011), NGC 1521 (Humphrey et al. 2012b), RXJ1159+5531 (Buote et al. 2016), and RXJ1416.4+2315 (Khosroshahi et al. 2006). We designate NGC 720 and NGC 1521 as “nearly” fossil systems since they obey the fossil classification within their projected virial radii, although typically they are classified as members of larger groups owing to more distant galaxy associations. There is presently newer and deeper *Chandra* and *Suzaku* data for the massive fossil cluster RXJ1416.4+2315 since the time of the initial analysis of a shallow *Chandra* observation by Khosroshahi et al. (2006). Our preliminary analysis incorporating all the available *Chandra* and *Suzaku* data yields a smaller concentration  $\sim 1\sigma$  below the mean  $c-M$  relation (Buote et al. 2016, in preparation). Our new measurement for NGC 6482 places it as the most extreme outlier in the  $c-M$  relation for fossils, with the next largest being NGC 720 ( $\sim 4\sigma$  with respect to the intrinsic scatter).

As noted above, if  $c_{200}$  for NGC 6482 is really  $> 30$  it would be a very rare system formed in  $\Lambda$ CDM, and perhaps its existence so near to us (i.e., representing a small cosmological search volume) would be difficult for  $\Lambda$ CDM to explain. The lower concentrations inferred by the AC models would mitigate any such tension with  $\Lambda$ CDM. While the standard AC prescriptions (AC1, AC2) yield  $M_*/L_K$  values for the BCG that are uncomfortably small compared to the SPS models, both AC models derived from cosmological simulations (AC3, AC4) are consistent with the SPS models. The “Forced Quenching” AC variant (AC4) gives the highest  $M_*/L_K$  of the AC models identical to that obtained for the un-contracted NFW model.

Additional support for the AC models comes from their lower baryon fractions in better agreement with the cosmic value once stellar baryons not associated with the BCG are considered (§6.6 and §8.2). Therefore, while AC4 still produces a significant outlier in the  $c-M$  relation (see Figure 12), we believe its advantages over the un-contracted NFW model and other AC models make it the preferred model of all those that we have investigated. The support for AC4 as opposed to AC1 or AC2 provides new evidence for “weak” AC and would seem to be consistent with stellar dynamics and lensing measurements of the mass profiles of early-type galaxies that favor no AC or weak AC (see §1; e.g., Dutton & Treu 2014). This is also generally consistent with the X-ray studies of a small number of massive elliptical galaxies and galaxy groups that somewhat disfavor AC1 and AC2 relative to no AC (see §1; H06; Gastaldello et al. 2007).

The qualitative features and conclusions of the above discussion also apply to when we use the Einasto profile for the DM. The principle difference is that the outlier significance is lessened somewhat with respect to NFW; e.g., the pure Einasto profile gives a  $c_{200}$  value that is  $4.2\sigma$  above the mean  $\Lambda$ CDM  $c-M$  relation in terms of the intrinsic scatter, and  $3.2\sigma$  above the mean for AC4. The lower outlier significance partially arises from the larger  $\Lambda$ CDM intrinsic scatter for the Einasto profile; i.e., 0.13 dex for Einasto vs. 0.11 dex for NFW (Dutton & Macciò 2014).

Finally, note that while the halo concentration of NGC 6482 is extreme compared to the other fossil systems, the  $R$ -band magnitude gap between the BCG and the next brightest member is quite typical for fossils (just over 2 magnitudes). In

fact, the  $R$ -band luminosity function of NGC 6482, as well as its color-magnitude relation, appear to be typical of the general group and cluster population (Lieder et al. 2013).

### 8.1.1. Theoretical Concentration-Mass Relation

When comparing the  $c_{200}$  we have measured from the X-ray data to theory, we have used the theoretical concentration-mass relations published by Dutton & Macciò (2014) for the following reasons. (1) It is a recent study using state-of-the-art numerical simulations with up-to-date cosmological parameters from *Planck*. (2) The study provides convenient power-law approximations to the  $c_{200}-M_{200}$  relation as a function of redshift for relaxed halos. (3) Results for both NFW and Einasto profiles are provided.

Moreover, the  $z \approx 0$   $c_{200}-M_{200}$  relations obtained by recent studies are quite consistent for our needs. For example, the double power-law approximation of Klypin et al. (2016) for relaxed, mass-selected,  $z = 0$  halos with  $M_{200} = 4.5 \times 10^{12} M_\odot$  gives  $c_{200} = 7.0$  compared to 7.2 which we obtain from the relation of Dutton & Macciò (2014) for  $z = 0$  halos. The relation of Klypin et al. (2016) gives a slightly larger value ( $c_{200} = 7.2$ ) for halos selected according to the maximum circular velocity (see Tables A1 and A2 of Klypin et al. 2016). Another example is provided by the recent study of Ludlow et al. (2016) who present the theoretical  $c_{200}-M_{200}$  relation for the Einasto profile as a function of  $z$ . Using the redshift and best-fitting Einasto mass of NGC 6482 (i.e.,  $M_{200} = 4.9 \times 10^{12} M_\odot$ ), we obtain  $c_{200} = 7.4$  for the relation published by Ludlow et al. (2016) compared to the value of 8.1 we obtain from Dutton & Macciò (2014).

Therefore, the uncertainties in the theoretical  $c_{200}-M_{200}$  relation at  $z \approx 0$  are considerably less than the statistical and systematic uncertainties associated with our measurement of  $c_{200}$  from the X-ray data. As a result, we do not discuss systematic differences in the theoretical relations henceforth in this paper.

### 8.2. Baryon Fraction

Whereas previously the global baryon fraction was effectively unconstrained for NGC 6482, with the addition of new *Suzaku* data and an improved hydrostatic modeling procedure we obtain  $f_{b,200} = 0.149 \pm 0.014$  (i.e.,  $\pm 9\%$  precision) for the fiducial hydrostatic model. As mentioned in §6.6 and §7.3, this value is very consistent with  $f_{b,U} = 0.155$ , but it only includes the stellar baryons from the BCG. Adding reasonable estimates for the non-BCG stellar baryons increases the baryon fraction to  $f_{b,200} \approx 0.19$ . This value marginally exceeds  $f_{b,U}$  ( $\sim 2.5\sigma$ ), and various systematic errors could lower the significance (Table 9). Nevertheless, the lower baryon fractions obtained for the AC models (Table 7) mitigate such tension with  $\Lambda$ CDM. For example, for AC4, considering only the BCG stellar bayons gives  $f_{b,200} = 0.136 \pm 0.016$  which rises to  $f_{b,200} \approx 0.18$  when including the non-BCG stars; i.e., only  $\sim 1.5\sigma$  above  $f_{b,U}$ . We conclude that the baryon fraction constraints favor the AC models. (To a lesser extent, they favor the Einasto model as well – see Table 9).

This solid evidence for a baryonically closed  $\approx 4.5 \times 10^{12} M_\odot$  halo associated with NGC 6482 has important implications for the “Missing Baryons Problem” at low redshift (Fukugita et al. 1998) as it suggests that, at least in massive elliptical galaxy / small group halos, many of the “missing” baryons can be located in the outer halo as part of the hot component – consistent with results we obtained previously for NGC 720 (Humphrey et al. 2011) and



NGC 1521 (Humphrey et al. 2012b). We emphasize, however, that the baryon fraction at  $r_{200}$  depends strongly on the form of the assumed DM profile (Table 9). For both the NFW and Einasto models (i.e., profiles consistent with  $\Lambda$ CDM simulations) baryonic closure is clearly indicated. However, the pseudo-isothermal CORELOG profile yields a much smaller value,  $f_{b,200} = 0.06 \pm 0.01$ . While the CORELOG profile is not motivated by the standard cosmological paradigm, it is consistent with the X-ray data of NGC 6482.

In addition to assumptions about the DM profile, the ability to measure  $f_{b,200}$  accurately for  $k_B T \lesssim 1$  keV systems like NGC 6482 is limited to a large extent by the accuracy of the iron abundance profile measured within  $r_{200}$ . As discussed in §7.8, for systems with  $k_B T \lesssim 1$  keV the plasma emissivity, and thus also the gas mass, are each very sensitive to the iron abundance at large radius where most of the gas mass resides (see the “ $\Lambda_\nu(T, Z)$ ” systematic error in Table 9). This issue is particularly relevant when considering that Anderson & Bregman (2014) found that  $\beta$ -model fits to the radial X-ray surface brightness profile of NGC 720 gave a value for the gas mass at  $r_{200}$  only about half of that we obtained in Humphrey et al. (2011) using essentially the same methodology as in our present investigation. While much of the difference undoubtedly can be attributed to the different model types employed in the two studies (e.g., the  $\beta$  model is equivalent to the CORELOG potential hosting isothermal hot gas – see, e.g., §2.1.1 of Buote & Humphrey 2012b), another key difference is that Anderson & Bregman (2014) assumed a constant metallicity  $Z = 0.6Z_\odot$  while Humphrey et al. (2011) assumed  $Z \approx 0.3Z_\odot$  for  $r \gtrsim r_{2500}$ . For  $k_B T \sim 0.5$  keV the factor of 2 higher metallicity assumed by Anderson & Bregman (2014) translates to a plasma emissivity higher by essentially the same factor and a gas mass that is lower by  $\approx \sqrt{2}$ .

### 8.3. Hydrostatic Equilibrium and the Stellar IMF

To directly quantify the accuracy of the hydrostatic equilibrium approximation requires measurements of the gas kinematics. In the central region of the Perseus cluster, which displays large cavities and other asymmetric features in the X-ray image presumed to arise from AGN feedback, *Hitomi* found somewhat surprisingly that the pressure from turbulence is only 4% of the thermal gas pressure (Hitomi Collaboration et al. 2016). If, as the *Hitomi* observation suggests, the hydrostatic equilibrium approximation is very accurate in a system like Perseus that possesses pronounced X-ray surface brightness irregularities, it also seems likely to be very accurate in NGC 6482 which exhibits a highly regular X-ray morphology (see §1). Consistent with an accurate hydrostatic equilibrium approximation, we find that plausible hydrostatic equilibrium models provide excellent fits to the X-ray data (§6.4) and the derived high halo concentration (§8.1) implies a system that is very old and is therefore highly evolved and relaxed.

The value of  $M_*/L_K$  that we obtain for the BCG from the hydrostatic equilibrium analysis agrees with SPS models that assume a Chabrier or Kroupa IMF and also favors a value for  $R_e$  close to the upper limit of the systematic range considered (see §5.2 and §6.4). Our measurement strongly disfavors a Salpeter IMF which predicts an  $M_*/L_K$  that is too high; i.e., even when using the upper limit for  $R_e$  (for the fiducial model and AC4) we obtain  $M_*/L_K \approx 0.89 \pm 0.11$  solar which is  $\approx 6\sigma$  smaller than the SPS value with a Salpeter IMF (1.58 solar). The clear preference for a

Chabrier or Kroupa IMF over Salpeter is consistent with our previous X-ray studies of massive elliptical galaxies, groups, and clusters (H06, Gastaldello et al. 2007; Humphrey et al. 2009a, 2012b; Buote et al. 2016) with the possible exception of NGC 720 (Humphrey et al. 2011). However, many other studies, particularly those that combine gravitational lensing and stellar dynamics, clearly favor the Salpeter IMF in massive early-type galaxies (e.g., Auger et al. 2010; Dutton et al. 2012; Conroy & van Dokkum 2012; Newman et al. 2013; Dutton & Treu 2014; Sonnenfeld et al. 2015).

The preference for different IMFs between the X-ray and lensing / stellar dynamical studies likely indicates an unappreciated large systematic error in one or both of the approaches. Since, other than the case of Perseus noted above, it has not been possible to accurately and precisely measure hot gas motions directly, it is natural to consider deviations from hydrostatic equilibrium as a leading candidate for a large systematic error. For NGC 6482, however, to account for the almost factor of 2 difference in the stellar mass implied by a Chabrier and Salpeter IMF would require a non-thermal gas pressure comparable to the thermal pressure. Given the evidence presented at the beginning of this section that NGC 6482 is very old and relaxed, we believe that such a large non-thermal pressure fraction is extremely unlikely. Nevertheless, resolving this IMF discrepancy provides additional motivation for obtaining measurements of hot gas motions of similar quality to Perseus for massive early-type galaxies.

### 8.4. Entropy Profile and Feedback

In §6.2 we found that for  $r \gtrsim r_{2500}$  the entropy profile we obtain for the fiducial hydrostatic model, when rescaled by  $\propto f_{\text{gas}}(< r)^{2/3}$ , diverges from the baseline  $\sim r^{1.1}$  entropy profile produced by cosmological simulations with only gravity, so that near  $r_{500}$  it nearly equals the original profile (see §6.2). This result is generic to all the DM models we investigated (NFW, Einasto, CORELOG, AC). Whereas the good matching of the rescaled profile to the baseline profile interior to  $\sim r_{2500}$  suggests feedback spatially rearranged the gas without heating it (as is found typically), the fact that the rescaled entropy exterior to  $\sim r_{2500}$  exceeds the baseline profile suggests the feedback raised the temperature of the gas in that region.

This behavior of the entropy profile is very similar to that of the nearly fossil system NGC 1521 (Humphrey et al. 2012b) which has a total mass very close to NGC 6482 and has gas temperature and density measurements extending out to  $r_{500}$ . The entropy profiles of NGC 6482 and NGC 1521 suggest possibly different feedback mechanisms shape the gas interior and exterior to  $\sim r_{2500}$  in those systems. But since other systems like NGC 720 do not display the same behavior (Humphrey et al. 2011), the feedback history is not universal. Measurements of the hot gas properties extending out to at least  $\sim r_{500}$  in more galaxies are needed to assess the generality of this result and its possible implications for galaxy formation.

## 9. CONCLUSIONS

In 2010 *Suzaku* observed NGC 6482 for a nominal 46.5 ks providing motivation for us to revisit its uncertain, but possibly extremely high, halo concentration inferred previously from a modest 20 ks *Chandra* observation (Khosroshahi et al. 2004; H06). NGC 6482 is an optimal target for analysis of its mass profile with X-ray observations because it is nearby



and fairly bright with a highly regular X-ray image that displays no evidence of a central AGN disturbance (see §1). Whereas our *Chandra* density and temperature profiles in H06 only extended to  $\sim 0.5r_{2500}$ , the *Suzaku* data allow these profiles to be measured fully out to  $r_{2500}$  leading to tighter constraints on the mass profile. The improved constraints partially arise from the addition of the *Suzaku* data but are also the result of our hydrostatic modeling approach having advanced since H06; i.e., we implement an “entropy-based” hydrostatic method that allows us easily to enforce the additional constraint of convective stability (e.g., Humphrey et al. 2008; Buote & Humphrey 2012a).

The fiducial hydrostatic equilibrium model we employ for our study has the following components: (1) reference pressure value at  $r = 1$  kpc; (2) entropy proxy profile consisting of a constant plus a broken power-law with two break radii; (3) stellar mass of the BCG represented by a Sersic model; (4) an NFW profile for the DM halo. The primary method we use to fit the hydrostatic equilibrium models to the data is Bayesian nested sampling. In addition, we employ a standard  $\chi^2$  minimization frequentist approach both to compare best-fitting parameters to the Bayesian values and for hypothesis testing.

The main results of our analysis are the following.

- **Extremely High Halo Concentration (§6.4, §8.1)** We measure  $c_{200} = 32.2 \pm 7.1$  and  $M_{200} = (4.5 \pm 0.6) \times 10^{12} M_{\odot}$  for the fiducial model. For a halo of this mass, the value we measure for  $c_{200}$  exceeds the expected value of  $c_{200} = 7.1$  for relaxed  $\Lambda$ CDM halos (Dutton & Macciò 2014) by  $3.5\sigma$  with respect to the statistical observational error, and by  $6\sigma$  considering the intrinsic scatter in the  $\Lambda$ CDM  $c-M$  relation. This measurement situates NGC 6482 as the most extreme outlier known for a fossil system. A  $6\sigma$  outlier in the  $c-M$  relation would represent an extremely rare object, possibly even too rare to form in  $\Lambda$ CDM simulations when taking into account the small cosmological sampling volume implied by the low redshift of NGC 6482. We believe this possible tension with  $\Lambda$ CDM favors AC models since they yield lower  $c_{200}$  values that are modestly less significant outliers in the  $c-M$  relation. We reach the same conclusions when using Einasto DM profiles instead of NFW though with modestly lower significances.
- **Weak Adiabatic Contraction (§5.4, §6.4, §8.1, §8.2)** We considered four variants of AC and applied them to the NFW and Einasto DM profiles. We found all the AC models fitted the data equally well in terms of a frequentist  $\chi^2$  analysis. Generally, the AC models give smaller  $M_*/L_K$ , smaller  $c_{200}$ , larger  $M_{200}$ , and smaller  $f_{b,200}$  than the un-contracted models. These parameter differences are strongest for the standard AC prescriptions (Blumenthal et al. 1986; Gnedin et al. 2004). We argue the X-ray analysis favors the *ad hoc* “Forced Quenching” AC model of Dutton et al. (2015), since not only does it have the advantages of producing smaller  $c_{200}$  and  $f_{b,200}$  than the un-contracted models, but it also yields the largest  $M_*/L_K$  of the AC models (equal to the un-contracted models) which agrees best with the stellar mass predicted by the SPS models. Support for AC that is weaker than the standard prescriptions is not inconsistent with other X-ray studies (H06;

Gastaldello et al. 2007) or stellar dynamics and lensing measurements (Dutton & Treu 2014) of the mass profiles of early-type galaxies (see §1).

- **Baryonically Closed (§6.6, §8.2)** We obtain  $f_{b,200} = 0.149 \pm 0.014$  very consistent with  $f_{b,U}$  for the fiducial model. When including estimates for the stellar baryons not associated with the BCG,  $f_{b,200}$  increases and marginally exceeds  $f_{b,U}$  ( $\sim 2.5\sigma$ ). For AC models the discrepancy is weaker ( $\lesssim 1.5\sigma$ ). The solid evidence for  $f_{b,200} \approx f_b$  in NGC 6482 indicates that at least some of the “Missing Baryons” at low redshift may be located in the outer regions of hot halos in massive elliptical galaxies.

Other notable results are as follows.

- **Surface Brightness and Temperature (§3)** The  $\Sigma_x$  and  $k_B T$  profiles obtained from *Chandra* and *Suzaku* agree well in their overlap region. At the largest radii ( $\sim r_{2500}$ ) there is weak evidence ( $\sim 1\sigma$ ) that the temperature profile turns around and begins to rise. Our measurements for *Chandra* differ significantly from H06 due to improvements in the atomic physics database used by the VAPEC plasma code.
- **Entropy (§6.2, §8.4)** Interior to  $\sim r_{2500}$  the radial profile of the entropy proxy displays evidence for feedback that has spatially rearranged the hot gas without heating it, very consistent with measurements of other galaxies, groups, and clusters. This is not the case exterior to  $\sim r_{2500}$ , where the entropy profile suggests that feedback has raised the gas temperature.
- **Pressure (§6.3)** The pressure profile of NGC 6482 broadly agrees with (considering the intrinsic scatter) the universal profile of galaxy clusters (Arnaud et al. 2010) for radii approximately  $0.1-0.7 r_{500}$ , but exceeds it elsewhere.
- **BCG Stellar Mass and the IMF (§6.4, §8.3)** The stellar mass we infer for the BCG, when allowing for plausible uncertainty in the assumed  $R_e$ , agrees with SPS models having a Chabrier or Kroupa IMF and strongly disfavors a Salpeter IMF. This result agrees with previous X-ray studies of massive elliptical galaxies, groups, and clusters but disagrees with results from many lensing and stellar dynamical studies. We argue that it is very unlikely the preference for a Chabrier/Kroupa IMF in NGC 6482 arises from a strong violation of the hydrostatic equilibrium approximation.
- **Dark Matter Profiles (§6.4)** The three DM profiles we investigated – NFW, Einasto, and a pseudo-isothermal logarithmic potential with a core (“CORELOG”) – all fit the data equally well in terms of a frequentist  $\chi^2$  analysis.
- **Slope of the Total Mass Profile (§6.5)** The total mass profile interior to  $\sim 2R_e$  is very close to a power-law with a mass-weighted density slope  $\langle\alpha\rangle = 2.00 \pm 0.04$ . Exterior to this radius the density profile steepens so that  $\langle\alpha\rangle = 2.27 \pm 0.09$  for  $r = 10R_e$ , which is  $\approx 12\%$  larger than the mean value of the  $\alpha-R_e$  scaling relation (Humphrey & Buote 2010) but is consistent within the observed scatter (Auger et al. 2010).

- **MOND (§6.7)** MOND is unable to explain the X-ray data without DM; e.g., at  $r \approx 35$  kpc the MOND DM fraction is  $0.68 \pm 0.05$  considering only the stellar baryons in the BCG which decreases to  $\approx 0.59$  when including plausible contributions from other stellar baryons. If we use the upper limit on  $R_e$  for the BCG, the DM fraction is reduced by an additional 0.09.

The properties we have measured for the dark and baryonic mass profiles of NGC 6482, particularly the extremely high halo concentration implying an ancient system, suggest it is a “classical” fossil group of the kind envisioned when the first fossil was discovered by Ponman et al. (1994).

I thank the anonymous referee for a constructively critical review that led to improvements in the manuscript. I also thank Dr. Melania Nynka for contributing software to assist with the spectral data analysis. I gratefully acknowledge partial support from the National Aeronautics and Space Administration (NASA) under Grant NNX15AM97G issued through the Astrophysics Data Analysis Program. Partial support for this work was also provided by NASA through Chandra Award Number GO4-15117X issued by the Chandra X-ray Observatory Center, which is operated by the Smithsonian Astrophysical Observatory for and on behalf of NASA under contract NAS8-03060. The scientific results reported in this article are based in part on observations made by the Chandra X-ray Observatory and by the Suzaku satellite, a collaborative mission between the space agencies of Japan (JAXA) and the USA (NASA). This research has made use of the NASA/IPAC Extragalactic Database (NED) which is operated by the Jet Propulsion Laboratory, California Institute of Technology, under contract with the National Aeronautics and Space Administration. We acknowledge the usage of the HyperLeda database.

## REFERENCES

- Alabi, A. B., Forbes, D. A., Romanowsky, A. J., et al. 2016, *MNRAS*, 460, 3838
- Alam, S. M. K., Bullock, J. S., & Weinberg, D. H. 2002, *ApJ*, 572, 34
- Anderson, M. E., & Bregman, J. N. 2014, *ApJ*, 785, 67
- Angus, G. W., Famaey, B., & Buote, D. A. 2008, *MNRAS*, 387, 1470
- Arnaud, K. A. 1996, in *Astronomical Society of the Pacific Conference Series*, Vol. 101, *Astronomical Data Analysis Software and Systems V*, ed. G. H. Jacoby & J. Barnes, 17
- Arnaud, M., Pratt, G. W., Piffaretti, R., et al. 2010, *A&A*, 517, A92
- Asplund, M., Grevesse, N., & Jacques Sauval, A. 2006, *Nuclear Physics A*, 777, 1
- Auger, M. W., Treu, T., Bolton, A. S., et al. 2010, *ApJ*, 724, 511
- Balucinska-Church, M., & McCammon, D. 1992, *ApJ*, 400, 699
- Bekenstein, J., & Milgrom, M. 1984, *ApJ*, 286, 7
- Blumenthal, G. R., Faber, S. M., Flores, R., & Primack, J. R. 1986, *ApJ*, 301, 27
- Brighenti, F., Mathews, W. G., Humphrey, P. J., & Buote, D. A. 2009, *ApJ*, 705, 1672
- Budzynski, J. M., Kuposov, S. E., McCarthy, I. G., & Belokurov, V. 2014, *MNRAS*, 437, 1362
- Bullock, J. S., Kolatt, T. S., Sigad, Y., et al. 2001, *MNRAS*, 321, 559
- Buote, D. A. 1999, *MNRAS*, 309, 685
- . 2000a, *ApJ*, 539, 172
- . 2000b, *MNRAS*, 311, 176
- Buote, D. A., Brighenti, F., & Mathews, W. G. 2004, *ApJ*, 607, L91
- Buote, D. A., & Canizares, C. R. 1994, *ApJ*, 427, 86
- Buote, D. A., & Fabian, A. C. 1998, *MNRAS*, 296, 977
- Buote, D. A., Gastaldello, F., Humphrey, P. J., et al. 2007, *ApJ*, 664, 123
- Buote, D. A., & Humphrey, P. J. 2012a, in *Astrophysics and Space Science Library*, Vol. 378, *Astrophysics and Space Science Library*, ed. D.-W. Kim & S. Pellegrini, 235
- Buote, D. A., & Humphrey, P. J. 2012b, *MNRAS*, 420, 1693
- . 2012c, *MNRAS*, 421, 1399
- Buote, D. A., Lewis, A. D., Brighenti, F., & Mathews, W. G. 2003a, *ApJ*, 594, 741
- . 2003b, *ApJ*, 595, 151
- Buote, D. A., Su, Y., Gastaldello, F., & Brighenti, F. 2016, *ApJ*, 826, 146
- Cappellari, M., Emsellem, E., Krajnović, D., et al. 2011, *MNRAS*, 413, 813
- Cappellari, M., Romanowsky, A. J., Brodie, J. P., et al. 2015, *ApJ*, 804, L21
- Cash, W. 1979, *ApJ*, 228, 939
- Chabrier, G. 2003, *ApJ*, 586, L133
- Ciotti, L., D’Ercole, A., Pellegrini, S., & Renzini, A. 1991, *ApJ*, 376, 380
- Conroy, C., & van Dokkum, P. G. 2012, *ApJ*, 760, 71
- Courteau, S., Cappellari, M., de Jong, R. S., et al. 2014, *Reviews of Modern Physics*, 86, 47
- Dariush, A., Khosroshahi, H. G., Ponman, T. J., et al. 2007, *MNRAS*, 382, 433
- David, L. P., Forman, W., & Jones, C. 1991, *ApJ*, 369, 121
- De Luca, A., & Molendi, S. 2004, *A&A*, 419, 837
- Démoclès, J., Pratt, G. W., Pierini, D., et al. 2010, *A&A*, 517, A52
- Diehl, S., & Statler, T. S. 2008, *ApJ*, 680, 897
- Dolag, K., Vazza, F., Brunetti, G., & Tormen, G. 2005, *MNRAS*, 364, 753
- D’Onghia, E., Sommer-Larsen, J., Romeo, A. D., et al. 2005, *ApJ*, 630, L109
- Dutton, A. A., & Macciò, A. V. 2014, *MNRAS*, 441, 3359
- Dutton, A. A., Macciò, A. V., Stinson, G. S., et al. 2015, *MNRAS*, 453, 2447
- Dutton, A. A., Mendel, J. T., & Simard, L. 2012, *MNRAS*, 422, 33
- Dutton, A. A., & Treu, T. 2014, *MNRAS*, 438, 3594
- Einasto, J. 1965, *Trudy Astrofizicheskogo Instituta Alma-Ata*, 5, 87
- Eke, V. R., Navarro, J. F., & Steinmetz, M. 2001, *ApJ*, 554, 114
- Ettori, S., Gastaldello, F., Leccardi, A., et al. 2010, *A&A*, 524, A68
- Feroz, F., Hobson, M. P., & Bridges, M. 2009, *MNRAS*, 398, 1601
- Fujimoto, R., Mitsuda, K., McCammon, D., et al. 2007, *PASJ*, 59, 133
- Fukugita, M., Hogan, C. J., & Peebles, P. J. E. 1998, *ApJ*, 503, 518
- Gastaldello, F., Buote, D. A., Humphrey, P. J., et al. 2007, *ApJ*, 669, 158
- Girardi, M., Aguerri, J. A. L., De Grandi, S., et al. 2014, *A&A*, 565, A115
- Gnedin, O. Y., Kravtsov, A. V., Klypin, A. A., & Nagai, D. 2004, *ApJ*, 616, 16
- González-Martín, O., Masegosa, J., Márquez, I., Guainazzi, M., & Jiménez-Bailón, E. 2009, *A&A*, 506, 1107
- Grevesse, N., & Sauval, A. J. 1998, *Space Science Reviews*, 85, 161
- Grillo, C. 2012, *ApJ*, 747, L15
- Harrison, C. D., Miller, C. J., Richards, J. W., et al. 2012, *ApJ*, 752, 12
- Hitomi Collaboration, Aharonian, F., Akamatsu, H., et al. 2016, *Nature*, 535, 117
- Ho, L. C., Greene, J. E., Filippenko, A. V., & Sargent, W. L. W. 2009, *ApJS*, 183, 1
- Humphrey, P. J., & Buote, D. A. 2008, *ApJ*, 689, 983
- . 2010, *MNRAS*, 403, 2143
- Humphrey, P. J., Buote, D. A., Brighenti, F., et al. 2012a, *ApJ*, 748, 11
- Humphrey, P. J., Buote, D. A., Brighenti, F., Gebhardt, K., & Mathews, W. G. 2008, *ApJ*, 683, 161
- . 2009a, *ApJ*, 703, 1257
- Humphrey, P. J., Buote, D. A., Canizares, C. R., Fabian, A. C., & Miller, J. M. 2011, *ApJ*, 729, 53
- Humphrey, P. J., Buote, D. A., Gastaldello, F., et al. 2006, *ApJ*, 646, 899
- Humphrey, P. J., Buote, D. A., O’Sullivan, E., & Ponman, T. J. 2012b, *ApJ*, 755, 166
- Humphrey, P. J., Liu, W., & Buote, D. A. 2009b, *ApJ*, 693, 822
- Ishisaki, Y., Maeda, Y., Fujimoto, R., et al. 2007, *PASJ*, 59, 113
- Jarrett, T. H., Chester, T., Cutri, R., et al. 2000, *AJ*, 119, 2498
- Jiang, G., & Kochanek, C. S. 2007, *ApJ*, 671, 1568
- Kalberla, P. M. W., Burton, W. B., Hartmann, D., et al. 2005, *A&A*, 440, 775
- Khosroshahi, H. G., Jones, L. R., & Ponman, T. J. 2004, *MNRAS*, 349, 1240
- Khosroshahi, H. G., Maughan, B. J., Ponman, T. J., & Jones, L. R. 2006, *MNRAS*, 369, 1211
- Klypin, A., Yepes, G., Gottlöber, S., Prada, F., & Heß, S. 2016, *MNRAS*, 457, 4340
- Kroupa, P. 2001, *MNRAS*, 322, 231
- Kuhlen, M., Strigari, L. E., Zentner, A. R., Bullock, J. S., & Primack, J. R. 2005, *MNRAS*, 357, 387
- Kundert, A., Gastaldello, F., D’Onghia, E., et al. 2015, *MNRAS*, 454, 161
- Kuntz, K. D., & Snowden, S. L. 2000, *ApJ*, 543, 195
- Lieder, S., Mieske, S., Sánchez-Janssen, R., et al. 2013, *A&A*, 559, A76
- Lodders, K. 2003, *ApJ*, 591, 1220
- Ludlow, A. D., Bose, S., Angulo, R. E., et al. 2016, *MNRAS*, 460, 1214
- Lumb, D. H., Warwick, R. S., Page, M., & De Luca, A. 2002, *A&A*, 389, 93
- Ma, C.-P., Greene, J. E., McConnell, N., et al. 2014, *ApJ*, 795, 158
- Macciò, A. V., Dutton, A. A., & van den Bosch, F. C. 2008, *MNRAS*, 391, 1940
- Mamon, G. A., & Łokas, E. L. 2005, *MNRAS*, 362, 95
- Marston, C. 1998, *MNRAS*, 300, 872
- McLaughlin, D. E. 1999, *AJ*, 117, 2398
- Merritt, D., Graham, A. W., Moore, B., Diemand, J., & Terzić, B. 2006, *AJ*, 132, 2685
- Milgrom, M. 1983, *ApJ*, 270, 365
- . 2015, *MNRAS*, 454, 3810
- Molendi, S., & Gastaldello, F. 2001, *A&A*, 375, L14
- Moretti, A., Pagani, C., Cusumano, G., et al. 2009, *A&A*, 493, 501
- Navarro, J. F., Frenk, C. S., & White, S. D. M. 1997, *ApJ*, 490, 493
- Newman, A. B., Ellis, R. S., & Treu, T. 2015, *ApJ*, 814, 26
- Newman, A. B., Treu, T., Ellis, R. S., et al. 2013, *ApJ*, 765, 24

- Nulsen, P. E. J., & Bohringer, H. 1995, *MNRAS*, 274, 1093
- Paggi, A., Fabbiano, G., Kim, D.-W., et al. 2014, *ApJ*, 787, 134
- Panagoulia, E. K., Fabian, A. C., Sanders, J. S., & Hlavacek-Larrondo, J. 2014, *MNRAS*, 444, 1236
- Planck Collaboration, Ade, P. A. R., Aghanim, N., et al. 2014, *A&A*, 571, A16
- Pointecouteau, E., & Silk, J. 2005, *MNRAS*, 364, 654
- Ponman, T. J., Allan, D. J., Jones, L. R., et al. 1994, *Nature*, 369, 462
- Pratt, G. W., Arnaud, M., Piffaretti, R., et al. 2010, *A&A*, 511, A85
- Raouf, M., Khosroshahi, H. G., & Dariush, A. 2016, *ApJ*, 824, 140
- Rasia, E., Borgani, S., Ettori, S., Mazzotta, P., & Meneghetti, M. 2013, *ApJ*, 776, 39
- Retana-Montenegro, E., van Hese, E., Gentile, G., Baes, M., & Frutos-Alfaro, F. 2012, *A&A*, 540, A70
- Sánchez-Blázquez, P., Gorgas, J., Cardiel, N., & González, J. J. 2006, *A&A*, 457, 809
- Sanders, R. H. 1999, *ApJ*, 512, L23
- Schmidt, R. W., & Allen, S. W. 2007, *MNRAS*, 379, 209
- Schneider, M. D., Frenk, C. S., & Cole, S. 2012, *J. Cosmology Astropart. Phys.*, 5, 030
- Shin, J., Woo, J.-H., & Mulchaey, J. S. 2016, *ArXiv e-prints*, arXiv:1610.03487
- Sonnenfeld, A., Treu, T., Gavazzi, R., et al. 2012, *ApJ*, 752, 163
- Sonnenfeld, A., Treu, T., Marshall, P. J., et al. 2015, *ApJ*, 800, 94
- Su, Y., Buote, D., Gastaldello, F., & Brighenti, F. 2015, *ApJ*, 805, 104
- Tozzi, P., & Norman, C. 2001, *ApJ*, 546, 63
- Tozzi, P., Rosati, P., Nonino, M., et al. 2001, *ApJ*, 562, 42
- Voit, G. M., Kay, S. T., & Bryan, G. L. 2005, *MNRAS*, 364, 909
- Zappacosta, L., Buote, D. A., Gastaldello, F., et al. 2006, *ApJ*, 650, 777
- Zhao, D. H., Jing, Y. P., Mo, H. J., & Börner, G. 2009, *ApJ*, 707, 354

